ETH  *IPP*

Institute for Particle Physics

ETHZ-IPP Internal Report 2001-06

September 2001

Diploma Thesis: Measurement of Electron-Beam-Parameters of the SLS Injection Accelerators

Daniel Oliver Sütterlin

Diploma Professor
Prof. Dr. Ralph Eichler, ETHZ/PSI

Supervision
Dr. Werner Joho, Dr. Leonid Rivkin, Dr. Volker Schlott, SLS/PSI

Content

1. Introduction

This thesis contains studies and measurements of the SLS injection accelerators.
Injection into the main accelerator, the booster synchrotron, is relatively difficult as it uses magnets with small gaps and a narrow vacuum chamber.
Therefore, the target of this work in particular is to point out possibilities for the improvement of the injection process into the booster, namely increasing the transmission through the transfer line to the booster and to enhance the injection efficiency into the booster itself. The considerations made are based on matching the beam envelope from the transfer line into the booster.

In order to achieve this goal it is necessary to describe the optic in the transfer line between the pre- and the main accelerator and to prove that these theoretical descriptions agree with measurements at the machine.
As the transfer line's optic depends clearly on initial conditions delivered by the pre-injector, these parameters need to be determined in advance. Simulations of the pre-injector will lead to a preferred set of reference parameters, which allow using a single setting for the quadrupole magnets of the transfer line to match with the booster.

This thesis is divided into four different sections:

Chapter two introduces the theoretical concepts of electron beam optics, which are needed for the description of the transversal dynamics of charged particles in an accelerator. These concepts form the basis for all further considerations.
The next section gives an overview of the SLS injection accelerators and points out special features as well as associated advantages and problems of the corresponding components.
The fourth chapter summarizes measurements performed on the machine, which are concluded in the final section.

2. Theoretical Considerations

This chapter introduces the basic theoretical approaches (called ***beam optics***, pioneered by ***Courant*** and ***Snyder***) in order to describe the transverse motion of a charged particle through an accelerator. See [1] and [2].

2.1. Movement of Charged Particles in Magnetic Fields

Any charged particle can be accelerated by an electric field $\vec{E}$ and is guided and focused by a magnetic field $\vec{B}$. The force acting on the particle of charge q and the velocity $\vec{v}$ is the ***Lorentz-Force*** $\vec{F}_{Lorentz} = q(\vec{E} + \vec{v} \times \vec{B})$.

Coordinate system:
The bending fields of an accelerator are usually directed vertically, causing the particle to follow a curved path (particle orbit) in the horizontal plane. A useful choice for a system of coordinates are therefore the local curvilinear coordinates:

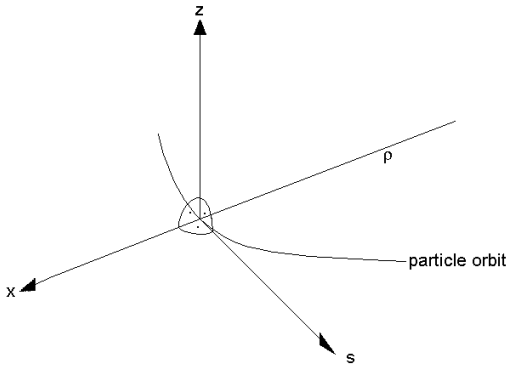

Fig. 2.1.1. Local curvilinear coordinates
The origin of the coordinates moves along with the particles' orbit.

- *(x,z)* transverse displacement from design orbit
- *s* path tangential along the central orbit
- ρ local radius of curvature

The local radius of curvature ρ of a charged particle moving in horizontal plane with velocity $\vec{v}$, in a magnetic guide field $\vec{B}$ is written as $\frac{e}{p} B_z(x,0,0) = \frac{1}{\rho}$ (1)

This result can easily be derived, as the particle traveling along the orbit does not move in the local curvilinear coordinates. It is therefore in a state of equilibrium, as the centrifugal force is compensated by the Lorentz-Force.

Result (1) suggests introducing a useful quantity called the ***magnetic rigidity (Bρ)*** [Tm].

$B\rho := \frac{p}{e}$. For a highly relativistic particle $B\rho = \frac{E}{c \cdot e} = \frac{V}{c}$. (2)

Numerically it applies that $\frac{B\rho[Tm]}{1Tm} \approx \frac{E[GeV]}{0.3} \cdot \frac{1}{1GeV}$.

Of course, a beam of particles enters the machine as a bundle of trajectories, which are centered on the ideal orbit. At any moment, a particle may be displaced horizontally or vertically from the ideal position. The transverse displacements are x and z. The particles may also have a divergence angle $x' := dx/ds$ and $z' := dz/ds$. This would cause them to get lost as they collide with the vacuum chamber, when there is no carefully shaped magnetic field, which restores them back towards the center of the beam, so that they start oscillating around the orbit.

By expanding B_z in terms of x and multiplying with $\frac{1}{B\rho}$ we achieve the following result for the horizontal motion:

$$\frac{1}{B\rho}B_z(x,z,s) = \underbrace{\frac{1}{B\rho}B_{z,0}}_{=\frac{1}{\rho}} + \underbrace{\frac{1}{B\rho}\frac{\partial B_z}{\partial x}\cdot x}_{=kx} + \underbrace{\frac{1}{2!}\frac{1}{B\rho}\frac{\partial^2 B_z}{\partial x^2}\cdot x^2}_{=\frac{1}{2!}mx^2} + \underbrace{\frac{1}{3!}\frac{1}{B\rho}\frac{\partial^3 B_z}{\partial x^3}\cdot x^3}_{=\frac{1}{3!}rx^3} + \ldots \qquad (3)$$

dipole quadrupole sextupole octupole

multipole	**definition**	**effect on the beam**
dipole	$\frac{1}{\rho} := \frac{1}{B\rho}B_{z,0}$	beam deflection
quadrupole	$k := \frac{1}{B\rho}\frac{\partial B_z}{\partial x}$	beam focusing
sextupole	$m := \frac{1}{B\rho}\frac{\partial^2 B_z}{\partial x^2}$	compensation of chromaticity
octupole	$r := \frac{1}{B\rho}\frac{\partial^3 B_z}{\partial x^3}$	field error, field compensation

The magnetic field around the beam can therefore be written as a sum of multipoles with different effects on the beam. By applying only the two lowest orders one speaks of ***linear beam-optics***, as only deflecting forces occur, which are either constant (dipole) or linear in transversal distance from the ideal orbit (quadrupole).

2.2. The Equation of Transversal Motion in Local Curvilinear Coordinates

Assuming that transversal motion is small and terms of second and higher order can be neglected (linear beam-optics) we find the equation of motion for the particle with some momentum deviation $\Delta p/p$ (p is the momentum defined by the magnetic rigidity) traveling through the lattice of an accelerator:

$$\frac{d^2x(s)}{ds^2} + \left[\frac{1}{\rho^2(s)} + k(s)\right]x(s) = \frac{1}{\rho(s)}\frac{\Delta p}{p} \qquad (4)$$

$$\frac{d^2z(s)}{ds^2} - k(s)z(s) = 0 \qquad (5)$$

Equations (4) and (5) represent the basic fundamentals describing ***linear beam-optics*** [1].

2.3. Transverse Dynamics

In the following sections the description of transverse motion is formulated, based on the fundamental equations (4) and (5). It is essential to distinguish straight sections where $1/\rho$ equals zero as well as bending magnets where the corresponding term does not vanish.

2.3.1. Beta Function and Betatron Oscillation

In a straight section equation (4) can be reformulated as

$$x''(s) + k(s)x(s) = 0 \qquad \textbf{(Hill's equation)} \tag{6}$$

Hill's equation describes an oscillation around the equilibrium orbit, as it represents a pseudo-harmonic oscillator with amplitude and phase depending on the position s along the beam.

The general solution of (6) can be written as:

$$x = a\sqrt{\beta(s)}\cos[\phi(s) - \phi_0] \tag{7}$$

The amplitude $a\sqrt{\beta(s)}$ is modulated with s, $\beta(s)$ is the **beta- or amplitude function**

and the phase advance is $\phi(s) = \int_0^s \frac{d\tilde{s}}{\beta(\tilde{s})}$, $a^2 = \varepsilon$ and ϕ_0 are constants (8)

2.3.2. Liouville's Theorem

By introducing the ***Twiss-parameters α and γ***, the constant factor $a^2 = \varepsilon$ can be calculated in terms of the displacement x and the divergence x':

$$\alpha := -\frac{1}{2}\frac{d\beta}{ds} \tag{9}$$

$$\gamma := \frac{1+\alpha^2}{\beta} \tag{10}$$

Equation (11) is called the ***Courant-Snyder-Invariant***

$$a^2 = \gamma x^2 + 2\alpha x x' + \beta x'^2 = \textit{constant} \tag{11}$$

Observing the x and x' values of a particle at a given point s, turn after turn, will paint an ellipse in phase space.

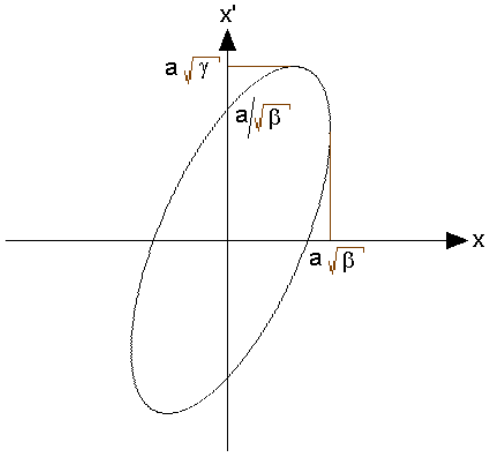

Fig. 2.3.2.1. Phase space ellipse

As a particle can be plotted as a point *(x, x')*, it may also be represented in *(q, p)* phase space. At a constant energy the two diagrams differ only by the scale of their axes. The area within the ellipse is proportional to the emittance ε. The area $A = \pi \cdot \varepsilon$ is expressed in units of π *mm mrad*.
The scaling of the axes is related by:
$p = \beta\gamma \cdot x'$
$q = x$
The normalized emittance is therefore introduced by writting $\varepsilon_{normalized} := \beta\gamma \cdot \varepsilon$.

Note: β and γ here are not the Twiss-parameters but the particle velocity in units of c and the Lorentz-factor.

Whatever focusing and bending operations are done on the particle, the emittance is conserved as long as the transverse momentum is constant. This is a direct consequence of the ***Theorem of Liouville***, which states that the particle density in phase space is constant for any particle described by canonical equations of motion. This corresponds with the demand that the particle moves in an external magnetic field in which the forces do not depend upon the particle velocity. The application of ***Liouville's theorem*** therefore is clearly ruled out when the particle emits synchrotron light or when space charge problems become dominating (e.g. at low energies).

2.3.3. Focusing Tune

An important parameter in circular machines, the ***tune***, is defined by:

$$Q := \frac{1}{2\pi} \oint \frac{ds}{\beta(s)} \tag{12}$$

Clearly, ***tune*** is the number of betatron-oscillations during one turn in the machine.

The importance of the tune lies in the fact, that any real machine contains errors in its lattice such as gradient (focusing) errors in quadrupoles, field errors in bending magnets, or field errors due to misalignment of quadrupoles.
Such errors lead to the fact that particles get lost, if appropriate resonance conditions are fulfilled:

$$mQ_x + nQ_y = p \qquad \text{m, n, p natural numbers} \tag{13}$$

error field	**resonant condition**	
dipole	$Q = p$	integer resonances
quadrupole	$2Q = p$	half - integer resonances
sextupole	$3Q = p$	third - integer resonances
octupole	$4Q = p$	fourth - integer resonances
…	…	…

This is illustratively explainable, if one states that particles spiral outwards in phase space if the perturbation has the same effect on each turn. The distortion from a dipole is independent of the transverse displacement *x* and can only build up in such a way if the particle returns to the same point in phase space on each turn. This condition is fulfilled for integer tunes. The error field of a quadrupole is linear to the displacement *x*. A particle making half turns in phase space will either see positive or negative kicks in the divergence *x'* but both will increase the growth of the error. This resonance will occur when tune equals to half integer values. [2]

2.3.4. Off Momentum Particle and Dispersion Function

In order to describe a particle with a non-vanishing impulse deviation $\delta := \Delta p / p$, $1/\rho$ should be different from zero, which means the equation must be solved only in bending magnets.
It helps to search a solution D(s) for equation (4) for $\delta = 1$ where (4) can be translated into:

$$\frac{d^2 D(s)}{ds^2} + \left[\frac{1}{\rho^2(s)} + k(s)\right] D(s) = \frac{1}{\rho(s)}$$, D(s) is called the **dispersion function**. (14)

A particle with a momentum deviation $\delta \neq 0$ will travel along a **disperse orbit** with a displacement $\boldsymbol{x_D = \delta \cdot D(s)}$ from the equilibrium orbit for $\delta = 0$. A particle with negative δ will be bent consistently too much in dipole magnets while the opposite occurs for positive δ. The particle will move on a shorter respectively on a longer orbit than a particle with a vanishing impulse deviation. This offset x_D is compensated by focusing forces, which drives the particle towards the equilibrium.

The horizontal position of the particle can therefore be written as follows:

$$x(s) = x_\beta(s) + x_D(s) = x_\beta(s) + D(s) \cdot \delta \quad (15)$$

where $x_\beta(s)$ is the betatron oscillation as solution of equation (6)

2.4. Matrix Description

An arbitrary section of the accelerator, which transports the particle from place to place, may be represented by a matrix. Any linear differential equation, like the Hill's equation has solutions, which can be traced from one point to another by a *2 x 2* matrix.

$$\begin{pmatrix} x_{final} \\ x'_{final} \end{pmatrix} = M \begin{pmatrix} x_{initial} \\ x'_{initial} \end{pmatrix} = \begin{pmatrix} m_{11} & m_{12} \\ m_{21} & m_{22} \end{pmatrix} \begin{pmatrix} x_{initial} \\ x'_{initial} \end{pmatrix} \quad (16)$$

This formalism can be represented analytically if the fields start and stop abruptly at the magnets end. This assumption of constant $1/\rho$ and k values over the entire length of the magnets leads to results which correspond well to reality.

Furthermore assuming that Liouville's theorem applies, it must be that the matrix determinant equals one, as any transformation should conserve the particle density in phase space. Therefore, the Twiss-parameters will transform as follows:

$$\begin{pmatrix} \beta_{final} \\ \alpha_{final} \\ \gamma_{final} \end{pmatrix} = \begin{pmatrix} m_{11}^2 & -2m_{11}m_{12} & m_{12}^2 \\ -m_{21}m_{11} & 1+2m_{12}m_{21} & -m_{12}m_{22} \\ m_{21}^2 & -2m_{22}m_{21} & m_{22}^2 \end{pmatrix} \begin{pmatrix} \beta_{initial} \\ \alpha_{initial} \\ \gamma_{initial} \end{pmatrix} \tag{17}$$

The transformation matrix M can also be determined if the Twiss-parameters are known at the begin and the end of a structure:

$$M = \begin{pmatrix} \sqrt{\frac{\beta_{final}}{\beta_{initial}}}(\cos\psi + \alpha_{initial}\sin\psi) & \sqrt{\beta_{initial}\beta_{final}}\sin\psi \\ \frac{(\alpha_{initial} - \alpha_{final})\cos\psi - (1+\alpha_{initial}\alpha_{final})\sin\psi}{\sqrt{\beta_{initial}\beta_{final}}} & \sqrt{\frac{\beta_{initial}}{\beta_{final}}}(\cos\psi - \alpha_{final}\sin\psi) \end{pmatrix} \tag{18}$$

where ψ is the phase advance between begin and end of the structure.

Stability in matrix terms is assured if $\begin{pmatrix} x \\ x' \end{pmatrix}_N = M^N \begin{pmatrix} x \\ x' \end{pmatrix}_{initial}$ remains finite for arbitrary large values of N. This corresponds to the demand that eigenvalues λ_1^N and λ_2^N must not grow with N. Therefore, the eigenvalues must be written as $\lambda_1 = e^{+i\mu}, \lambda_2 = e^{-i\mu}$. To obtain stability μ must be real. With $Tr(M) = \lambda_1 + \lambda_2 = 2\cos(\mu)$, it must be that $-1 \le \frac{Tr(M)}{2} \le 1$.

2.5. Beam Size and Emittance

So far, we have been dealing only with a single charged particle. An electron bunch however, contains several particles; each of them describes a transverse motion with some amplitude. Assuming an equilibrium (gaussian) distribution of the particles, we write for the transverse charge density:

$$\rho(x,z) = \frac{Ne}{2\pi\sigma_x\sigma_z} e^{-\left[\frac{x^2}{2\sigma_x^2} + \frac{z^2}{2\sigma_z^2}\right]} \tag{19}$$

with N the number of particles within the bunch.
The standard deviations σ_x and σ_z are called the horizontal, respectively the vertical rms beam sizes, given by $\sigma(s) = \sqrt{\varepsilon \cdot \beta(s)}$ (20)

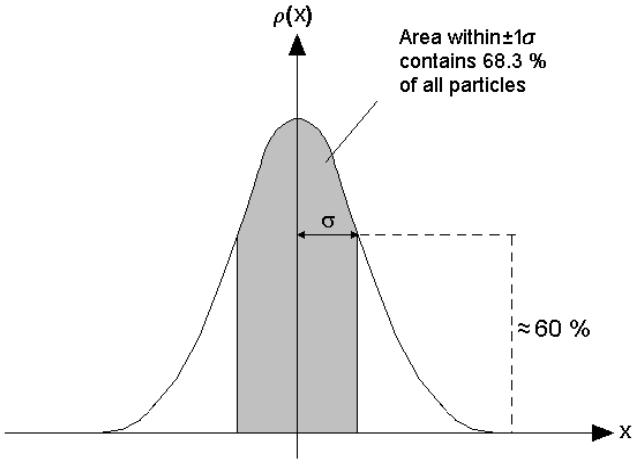

Fig. 2.5.1. Horizontal distribution of the beam bunch

The emittance of the entire beam therefore can be defined by

$$\varepsilon_{beam} := \frac{\sigma^2}{\beta(s)} \tag{21}$$

The total beam size Σ is given by $\Sigma^2 = \sigma^2 + \sigma_\varepsilon^2 = \sigma^2 + D^2\delta^2$ (22)

if an equilibrium energy distribution in the bunch is taken into account.

In all further considerations a ***gaussian distribution*** in both transverse and longitudinal phase space is assumed.

The theoretical concepts introduced in the above chapter are the basis for all considerations in the following sections. Therefore, reference to above-mentioned equations is taken by using their numbers.

3. Overview of the SLS Injection Accelerators

The SLS is a third generation synchrotron light source. It consists of a 100 MeV pre-injector linear accelerator (LINAC), a linac to booster transfer line (LTB), a full energy booster synchrotron, a booster to storage ring transfer line (BTR) and a 2.4 GeV storage ring. As a new feature, the booster and the storage ring are placed in the same tunnel. Thanks to its large circumference and correspondingly high number of bending magnets, the booster synchrotron delivers a beam with a very small emittance at 2.4 GeV. As a consequence, this allows the use of a small vacuum chamber and small gap magnets , but also makes it difficult to inject at 100 MeV.
The SLS is designed to provide synchrotron light of an extremely high brightness and therefore has very high phase space density of stored electrons. This leads to comparatively short lifetimes of the stored beam, due to intra-beam scattering. The current in the SLS storage ring is kept at a constant and high level using top-up injection, which necessitates efficient injection into the storage ring.

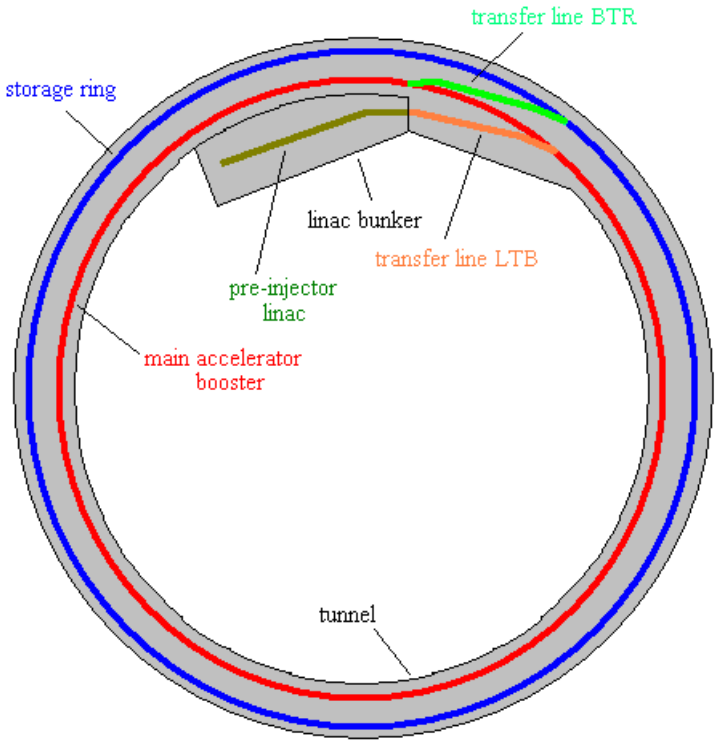

Fig. 3. 1. Overview of the SLS machine complex

3.1. The SLS Pre-Injector Linac

A key part of the injection is the pre-injector (LINAC), consisting of a 90 kV thermionic electron gun, which is pulsed with a repetition rate of 500 MHz, a bunching section and a 100 MeV linear accelerator.
The bunching section combines a 500 MHz sub-harmonic pre-buncher and two separate 3 GHZ traveling wave-bunchers. The linac itself consists of two 50 MeV, 3 GHz accelerating structures with a quadrupole triplet in between in order to allow beam matching to the second accelerating structure [3].

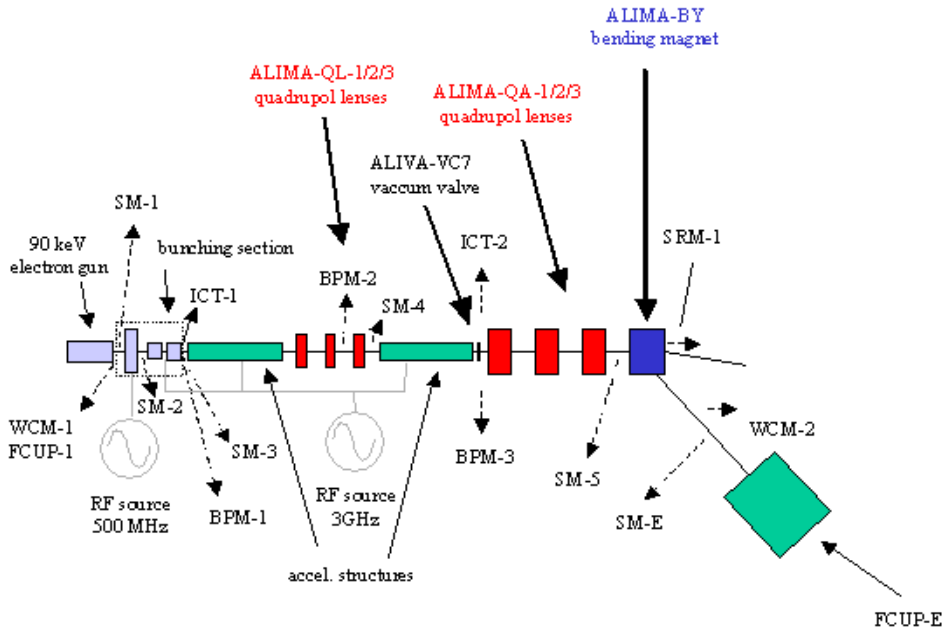

Fig. 3.1.1. Schematic overview of the SLS pre-injector

3.1.1. Beam Diagnostics in the Pre-Injector and Concept of Beam Parameter Measurements

The integrating current transformers ***ALIDI-ICT-1/2*** (see appendix part 4) situated in front of the first, respectively after the second structure, constantly monitor beam charge in and transmission through the linac.
Screen monitors allow measurement of the transverse beam parameters. Optical functions and emittance are usually measured at screen monitor ***ALIDI-SM-5*** behind the linac using the ***emittance measurement application (emm)*** [4] written in language ***IDL 5.1*** [5]. Horizontal and vertical beam sizes are taken at ***ALIDI-SM-5*** while the quadrupole triplet ***ALIMA-QA-1/2/3*** is being altered. As a special feature ***emm*** keeps beam sizes within certain limits. Assuming that only linear beam optics is relevant, the matrix formalism is applicable, therefore it can be written in both the horizontal and vertical plane $\beta_{SM-5}^{x,z} = \beta_0^{x,z} m_{11}^2 - 2\alpha_0^{x.z} m_{11} m_{12} + \frac{1+(\alpha_0^{x,z})^2}{\beta_0^{x,z}} m_{12}^2$ (see eq. (17)). $\alpha_0^{x,z}$, $\beta_0^{x,z}$ are the optical functions at the linac exit. The matrix elements m_{ik} depend on the focusing strengths of the used quadrupoles, and therefore on the currents applied to these.
As the screen monitor ***SM-5*** is placed in front of the first bending magnet, dispersion equals zero. According to (21) beam sizes are given by $\sigma_{SM-5}^{x,z} = \sqrt{\beta_{SM-5}^{x.z} \varepsilon^{x,z}}$. By measuring N times the beam size for N different matrices M (different currents in the quadrupoles) allows to compute the parameters $\alpha_0^{x,z}$, $\beta_0^{x,z}$ and $\varepsilon^{x,z}$ by using a ***χ^2 fit***.
In order to allow determination of variance it is best to perform several measurements in a row and then calculate the arithmetic average of the values $\bar{x}$ and the standard deviation

$\sqrt{\frac{1}{n-1}\sum_i (\bar{x} - x_i)^2}$, with n = *numbers of measurements*.

The energy spread of the 100 MeV beam can be measured at the screen monitor
ALIDI-SM-E, situated in front of the linac beam-dump. As beta functions and emittances are known from the emittance measurement behind the linac (and dispersion can be calculated), the

energy spread can be determined when measuring the horizontal beam distribution $\Sigma = \sqrt{\varepsilon \cdot \beta + D^2 \cdot \delta^2}$ at ***SM-E***.
It is preferable to switch off the ***QE*** quadrupole, which results in a small horizontal beta function and large dispersion at ***SM-E*** and therefore increases resolution of the measurement.

3.1.2. Optical Functions in Second Linac Structure

In order to achieve good injection efficiency from the linac into the booster through LTB, the optical functions of the transfer line should match those in the booster.

In the following, some descriptive considerations are made in order to derive optical functions at the end of the linac, which determine the initial condition for the LTB matching simulations.

Considering the second linac structure: the beam doubles its energy from 50 MeV to 100 MeV. We assume a drift from one end of the structure to the other.
For optimization of transmission through the structure, we minimize the beta function in it.

Therefore, set $\sigma_{initial} \approx \sigma_{final}$ by adjusting the quadrupoles ***ALIMA-QL-1/2/3*** between the two linac structures.

$$\sigma^2_{initial} = \varepsilon_{initial} \cdot \beta_{initial}$$
$$\sigma^2_{final} = \varepsilon_{final} \cdot \beta_{final}$$

Since we double the energy, we write $\varepsilon_{final} = \frac{\varepsilon_{initial}}{2}$ which results in:

$$\beta_{final} = 2 \cdot \beta_{initial} \tag{23}$$

Recalling equation (17)

$$\beta_0 \equiv \beta_{initial}$$
$$\beta = \left(m_{11}^2\right)\beta_0 + (-2m_{11}m_{12})\alpha_0 + \left(m_{12}^2\right)\gamma_0 \tag{24}$$
$$\alpha = -m_{21}m_{11}\beta_0 + (1 + 2m_{12}m_{21})\alpha_0 - m_{12}m_{22}\gamma_0$$

Using the matrix for a drift space $M = \begin{pmatrix} m_{11} & m_{12} \\ m_{21} & m_{22} \end{pmatrix} = \begin{pmatrix} 1 & L \\ 0 & 1 \end{pmatrix}$ we write:

$$\begin{aligned} \beta &= \beta_0 - 2L\alpha_0 + L^2\gamma_0 \\ \alpha &= \alpha_0 - L\gamma_0 \\ \beta(s) &= \beta_0 - 2s\alpha_0 + s^2\gamma_0 \end{aligned} \tag{25}$$

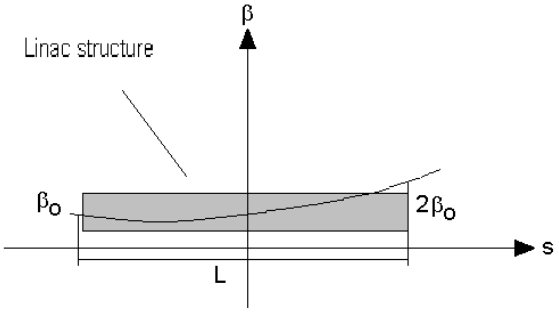

Fig. 3.1.2.1. Beta function in second linac structure

The second accelerator structure is assumed as drift space, as $\varepsilon_{final} = ½ \cdot \varepsilon_{initial}$, therefore it must be that $\beta_{initial} = 2 \cdot \beta_0$ when equal beam sizes are desired at both ends.

According to (23) it is

$\beta(L) = 2\beta_0 = \beta_0 - 2L\alpha_0 + L^2\gamma_0$. By inserting the definition of the Twiss-parameter γ_0 we find

$$\beta_0 = L\left(-\alpha_0 + \sqrt{2\alpha_0^2 + 1}\right). \tag{26}$$

By minimizing β_0 for an initial α_0 we get the following result for the beta- and alpha functions:

$$\begin{aligned} \alpha &= -\sqrt{2} \\ \beta &= \sqrt{2}L \end{aligned} \quad \text{with L = 5 m} \quad \begin{aligned} \alpha &\approx -1.5 \\ \beta &\approx 7m \end{aligned} \tag{27}$$

This set of parameters was confirmed by comparison of beam dynamics simulation codes such as ***AGILE*** [6] and ***TRANSPORT*** [7]. While ***TRANSPORT*** takes the acceleration in the second linac structure into account, ***AGILE*** considers it as a drift space similar to the initial thoughts.

The following simulations are shown for three measured sets of parameters at the linac exit, which are:

Reference condition: β = 7 m, α = -1.5
Condition 1: β = 12 m, α = -2.5
Condition 2: β = 3 m, α = -0.75

In the simulation the focusing strength of the quadrupole lenses in between the two linac structures is a function of the currents applied to them:

ALIMA-QL-1: 1.40 A
ALIMA-QL-2: 2.80 A
ALIMA-QL-3: 1.40 A

The resulting focusing strength k is given by $k = t_{lin} \cdot I_{Quad}$ with the linear factor $t_{lin} = \frac{2\mu_0 n}{a^2} \cdot \frac{1}{B\rho}$.

[1]

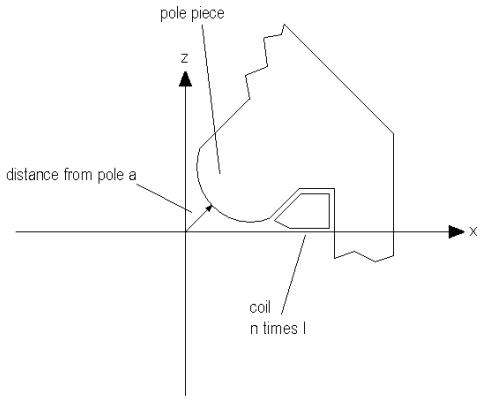

Fig. 3.1.2.2. Quadrupole magnet ALIMA-QL
a = 21 mm, n = 120 windings per pole.
For an energy of 50 MeV we find t_{lin} = 4.1 $m^{-2}A^{-1}$.

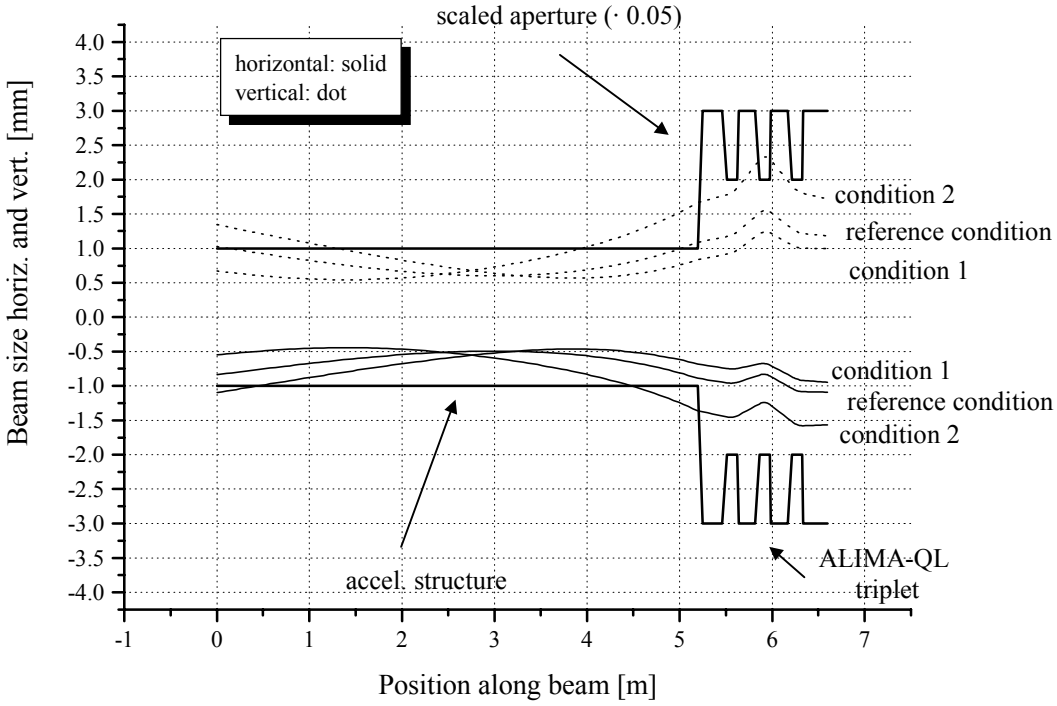

Fig. 3.1.2.3. Horizontal and vertical beam size (1σ) in second linac structure, calculated backwards from linac exit with AGILE, assuming the second structure as drift space
Emittance$_x$ = 0.10 mm mrad, emittance$_z$ = 0.15 mm mrad (at 100 MeV) corresponding to a representive measurement. The emittance at the end of the structure (100 MeV) is only half of the emittance at the start (50 MeV); the decrease is exponential.

The same calculation however with acceleration in the structure, using the ***TRANSPORT*** code:

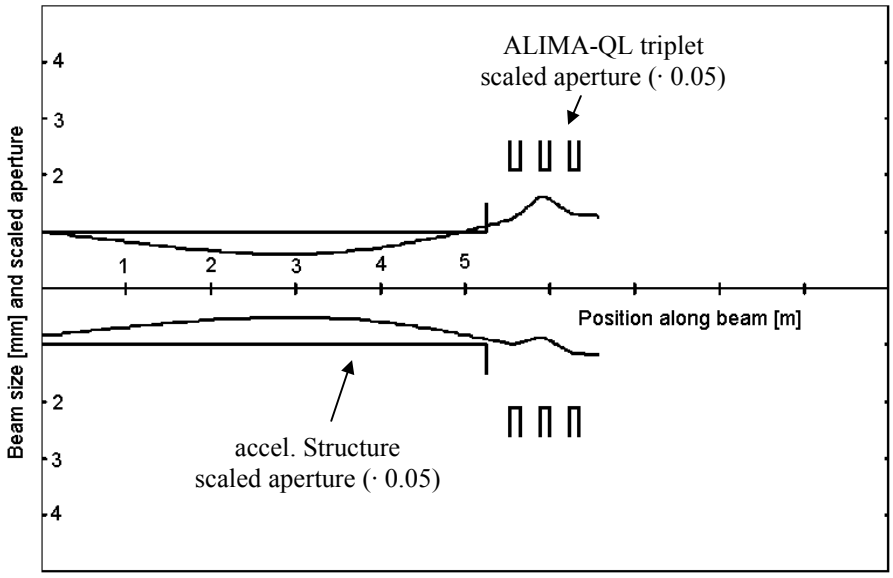

Fig. 3.1.2.4. Beam sizes (1σ) calculated backwards from linac exit with TRANSPORT for reference condition
Upper curve is the vertical, lower curve the horizontal beam size

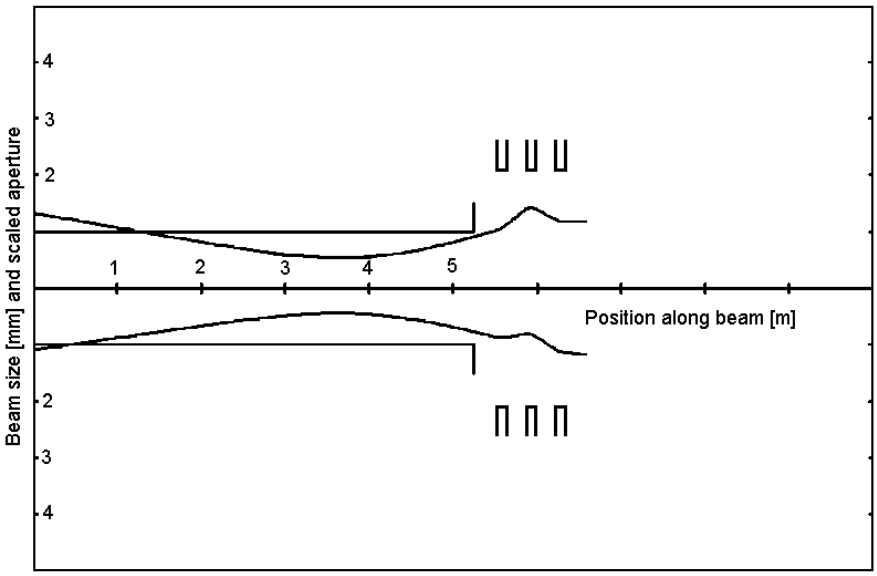

Fig. 3.1.2.5. Beam sizes (1σ) calculated backwards from linac exit with TRANSPORT for condition 1

Upper curve is the vertical, lower curve the horizontal beam size

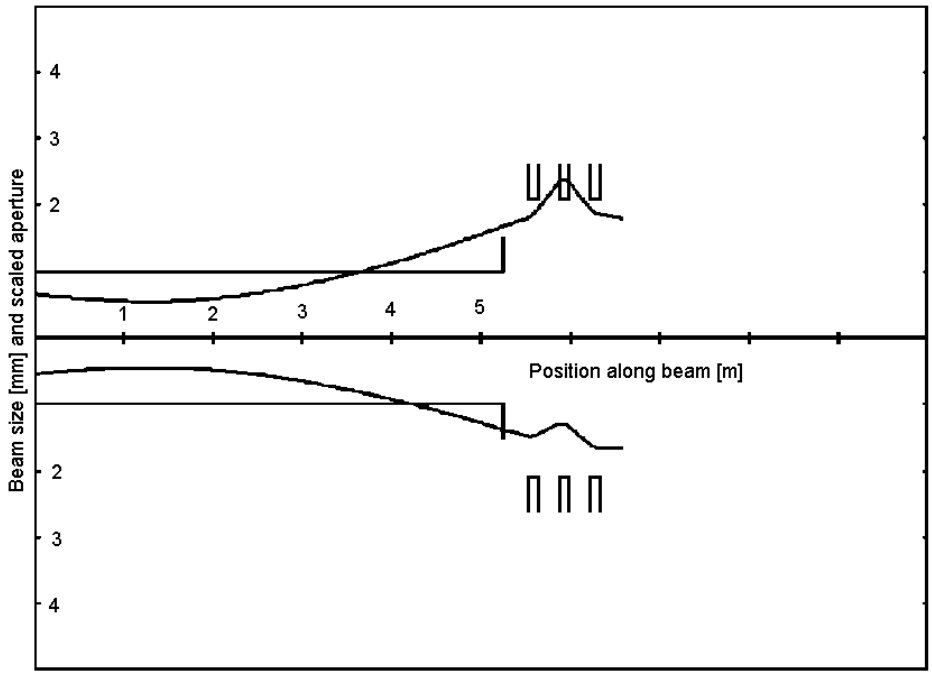

Fig. 3.1.2.6. Beam sizes (1σ) calculated backwards from linac exit with TRANSPORT for condition 2

Upper curve is the vertical, lower curve the horizontal beam size

The simulations executed with both codes support the assumption of the second linac structure as drift space. The parameters in (27) will be used in the following as reference conditions at the end of the linac. This point is named as valve ***ALIVA-VC7***.

The main reason for differing beam parameters at ***ALIVA-VC7*** are due to the subharmonic pre-buncher, which suffers from multi-pactoring causing quite unstable beam conditions and transmission through the linac (see figure 4.4.1.). Therefore, optimization needs to be done in regular time intervals by adjusting RF phases within the bunching section [3]. Especially after periods of machine shutdown values of optical functions may differ from those prior to the shutdown by a factor of two or even larger. This effect can be simulated and confirmed by the ***PARMELA*** code [8].
A new 500 MHz subharmonic pre-buncher cavity is presently built by the provider of the linac ACCEL and will be installed by the end of this year. As a matter of fact, more stable beam conditions corresponding to the calculated parameters at the linac exit can be expected. Therefore, matching of the LTB is expected to be non-changing in the future and will comply with the theoretical considerations made in this chapter.

3.2. The Transfer Line Linac to Booster LTB

Figure 3.2.1. gives a schematic overview of the LTB with all available diagnostic instrumentations. ICT's [4] at the beginning and the end of the LTB are used for monitoring transmission through the LTB, while the screen monitors allow visualizing the transverse dimensions of the beam. In addition, three BPM's can be used for online monitoring of beam positions. The $\Delta E/E$ distribution through LTB can be limited by using the horizontal scraper ***HS***, acting together with the ***BY*** bending magnet as an energy filter.

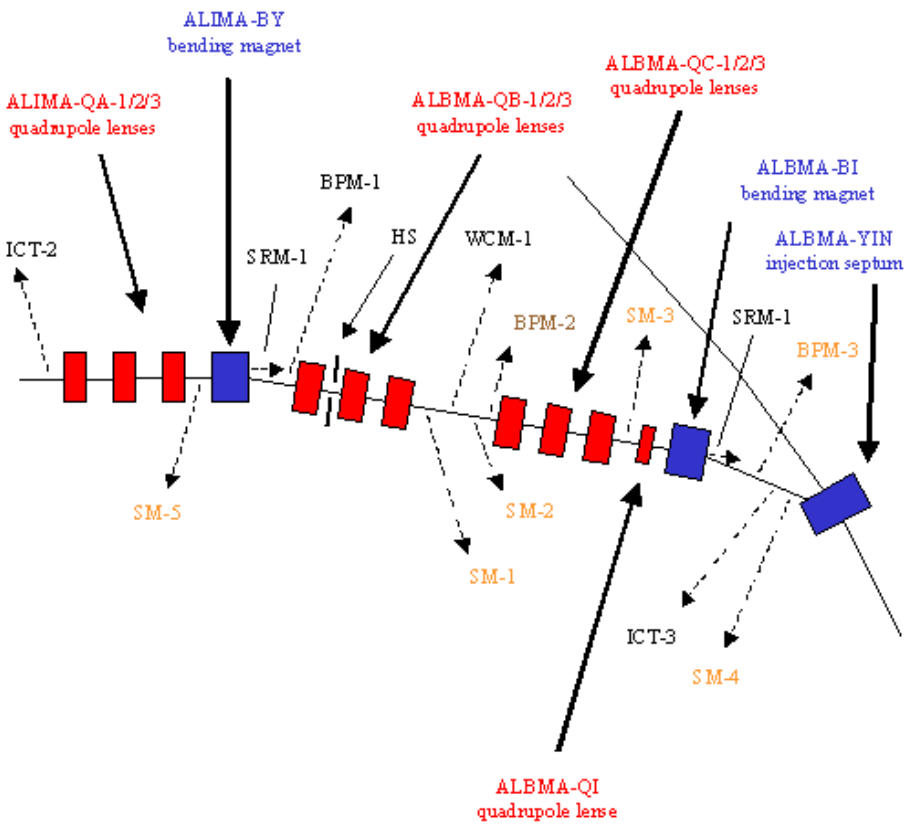

Fig. 3.2.1. Schematic overview of the LTB transfer line

3.2.1. Simulation of Optical Functions in LTB

The optical functions were calculated with different codes, using the matrix formalism mentioned in chapter 2. Most of these codes comprise numerical matching methods, which allow the achievement of desired optical parameters at a given point (e.g. the end of a transfer line) with the focusing strength of quadrupoles as variables. The code used for the simulations in this thesis was ***AGILE***. Comparison of results with those from other codes such as ***OPA*** [9] for the same input parameters indicates good agreement.

The LTB was matched to the end of one third of the booster lattice. It was found that this procedure minimized the discrepancies to the booster design lattice.
The matching is presented for the reference initial conditions at ***ALIVA-VC7***, calculated in chapter 3.1.2. The optical functions at the location of the screen monitors are shown in table 3.2.1.1. In the following table the magnet setting of the quadrupoles including both parameters, the focusing strength of the corresponding quadrupole and the current being applied to it, is presented.

Table 3.2.1.1. Optical functions in the LTB simulated with AGILE for reference setting according to calculation in chapter 3.1.2.

Opt. function	Screen monitor ALIDI-SM-5	Screen monitor ALBDI-SM-1	Screen monitor ALBDI-SM-2	Screen monitor ALBDI-SM-3	Screen monitor ALBDI-SM-4
β_x [m]	6.87	4.37	4.22	7.40	4.12
α_x	1.59	0.80	-0.76	1.28	0.20
β_z [m]	0.59	6.28	5.43	4.14	3.97
α_z	-0.61	0.53	-0.32	-0.05	0.08
D_x [m]	0.00	1.02	0.96	0.69	0.10
dD_x/ds [rad]	0.00	-0.01	-0.01	-0.32	-0.14

Table 3.2.1.2. Calculated focusing strengths and currents for reference setting

Magnet	k [m^{-2}]	I [A]
ALIMA-QA-1	-6.259	-30.833
ALIMA-QA-2	8.242	40.601
ALIMA-QA-3	-7.575	-37.315
ALBMA-QB-1	0.099	0.488
ALBMA-QB-2	-4.446	-21.901
ALBMA-QB-3	3.705	18.251
ALBMA-QC-1	1.628	8.020
ALBMA-QC-2	-4.209	-20.734
ALBMA-QC-3	3.363	16.567
ALBMA-QI	-0.300	-0.840

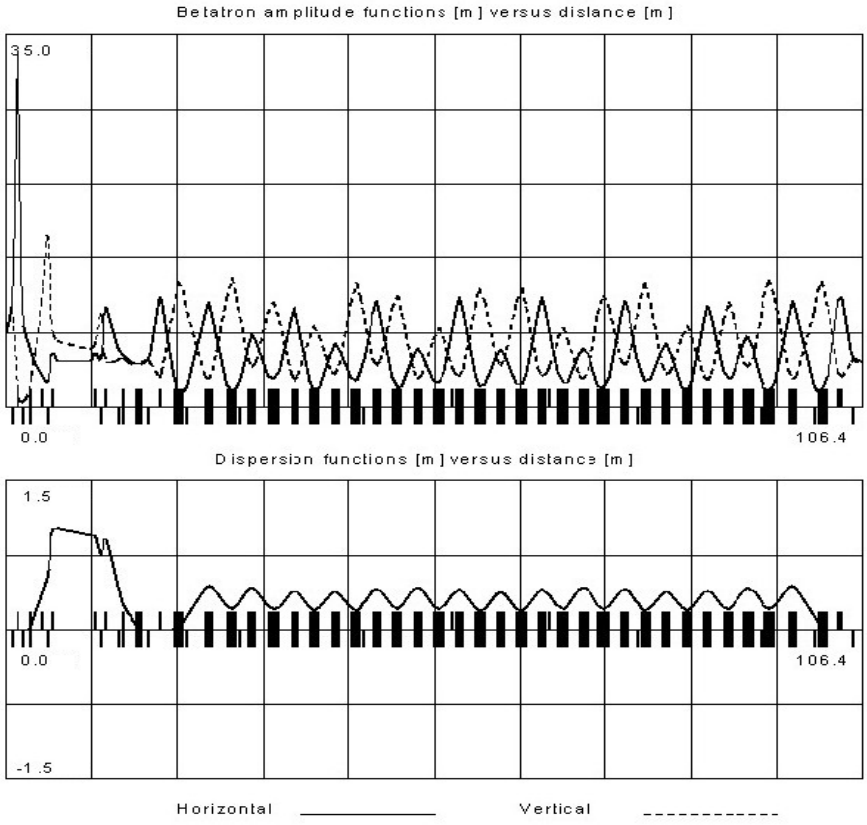

Fig. 3.2.1.1. Display of optical functions along LTB plus one third of booster using GUI
Initial values are, $\beta_{x,z}$= 7 m and $\alpha_{x,z}$= -1.5

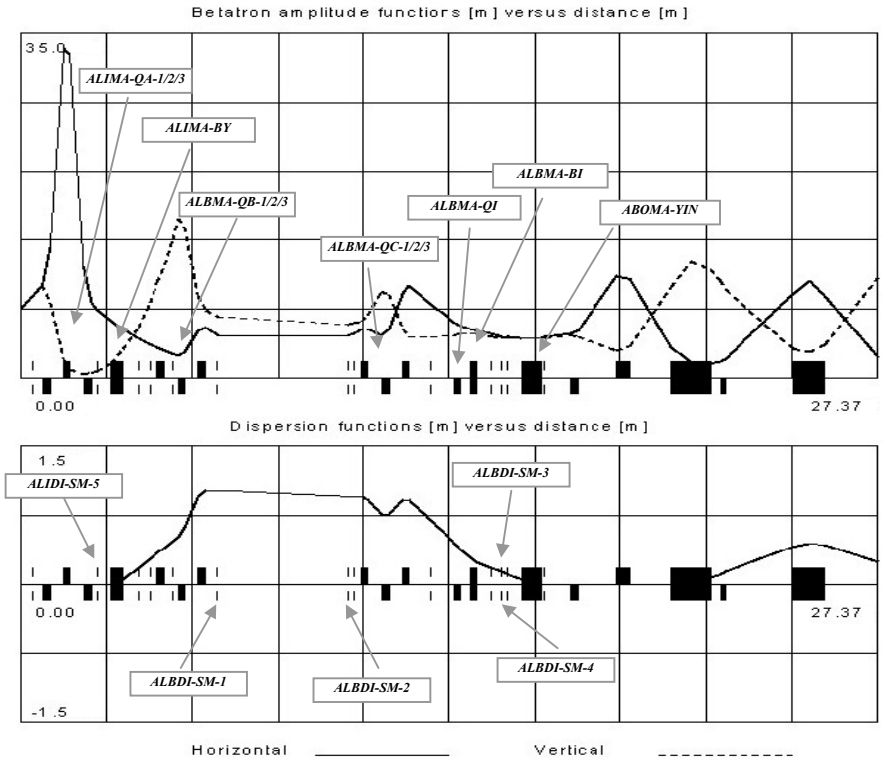

Fig. 3.2.1.2. Display of optical functions along LTB up to booster entrance using GUI
Initial values are, $\beta_{x,z}$= 7 m and $\alpha_{x,z}$= -1.5

Since quite different beam conditions have been measured behind the linac, due to instabilities and phase drifts in the 500 MHz sub-harmonic pre-buncher, several matching settings through LTB have been used. The settings for other initial conditions are listed in the appendix. Each of these settings leads to good transmission through the LTB and good matching of the injection parameters. Normal transmission rate through LTB is around 85 %, while injection efficiency is less than 80 % (see section 4.4.). Improvements of 10 % were achievable for both the transmission rate through the LTB as well as the injection efficiency.
Still, it is preferable to operate a single magnet setting for the LTB, such as the one calculated for the reference conditions and to adjust the linac parameters accordingly. Such a procedure is applicable as soon as the 500 MHz sub-harmonic pre-buncher is exchanged and the linac delivers stable beam conditions.

3.3. The Booster

The booster synchrotron is the main accelerator of the SLS complex; it accelerates electrons from the linac's energy of 100 MeV up to the SLS design energy of 2.4 GeV [10].
The design of the booster was driven by an unusual concept: 93 combined dipole/quadrupole/ sextupole magnets were installed in the same tunnel as the storage ring, resulting in a large circumference of 270 m. Two of the three dispersion free straight sections serve to accommodate the accelerating cavity and the injection elements.
Additional quadrupoles in these places are used for the variation of the tunes.
The booster lattice leads to an extremely small emittance and small dispersion values. Therefore, vacuum chambers of small size and narrow magnetic gaps can be used. This leads to small operating costs as well as excellent quality of the extracted beam, but makes a clean injection into the booster itself necessary.

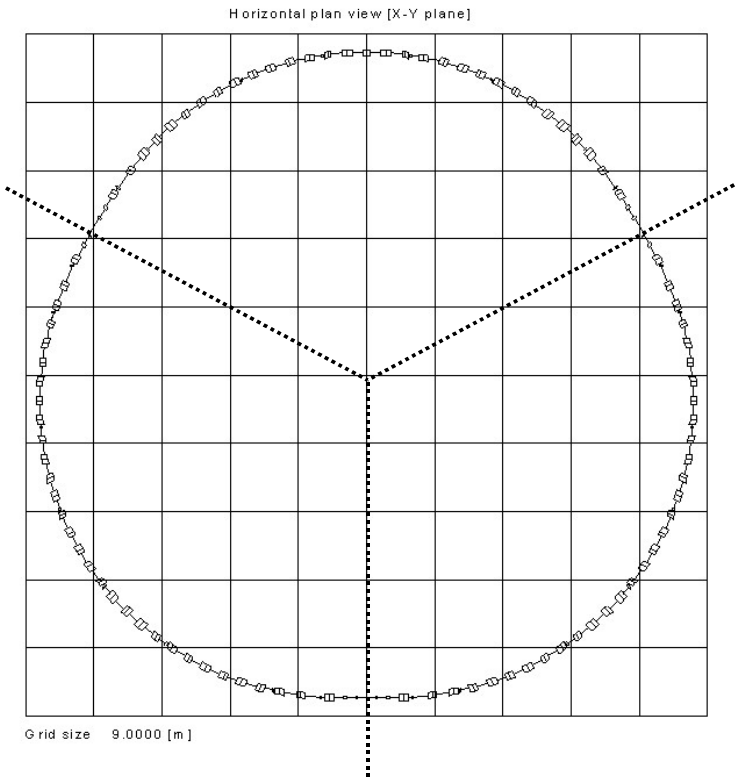

Fig. 3.3.1 Booster magnet-structure
The Booster latticee can be subdivided into three equivalent sections, each with mirror symmetry.

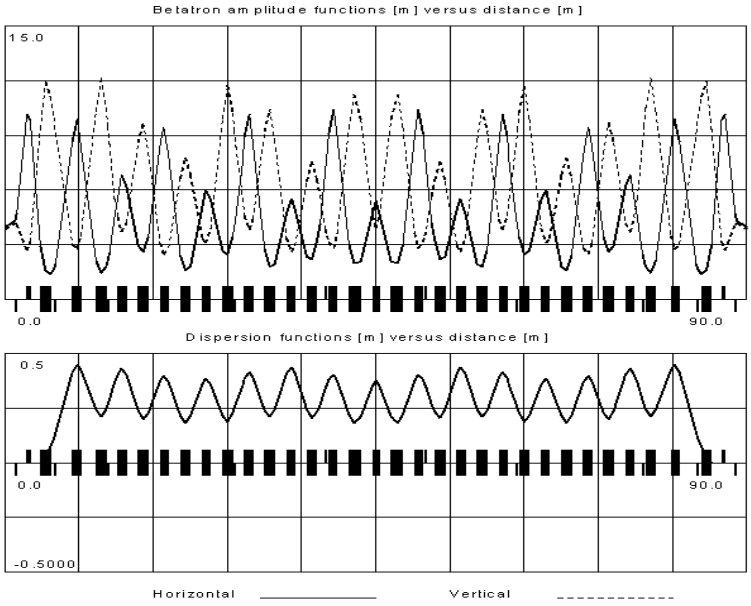

Fig. 3.3.2 Optical functions for one third of the booster design lattice
The other two third look the same; all three are connected through dispersion free straight sections

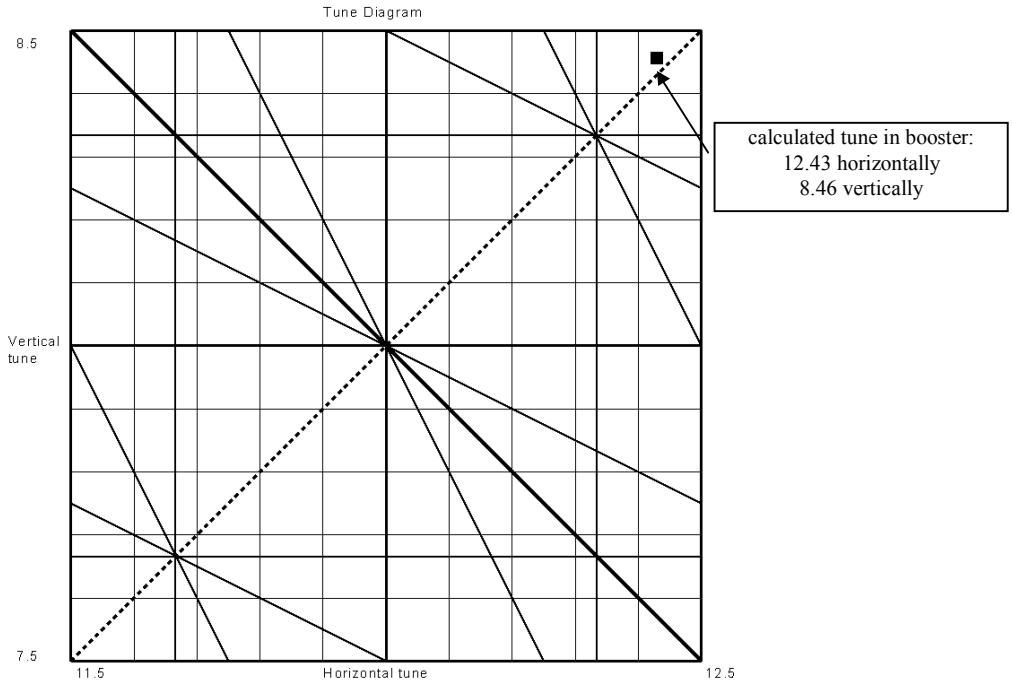

Fig. 3.3.3. Tune diagram for booster lattice up to 3rd order resonances

4. Measurement of Beam Parameters

All measurements of transverse beam parameters were performed using screen monitors. The following description shows the principles of the measurements:

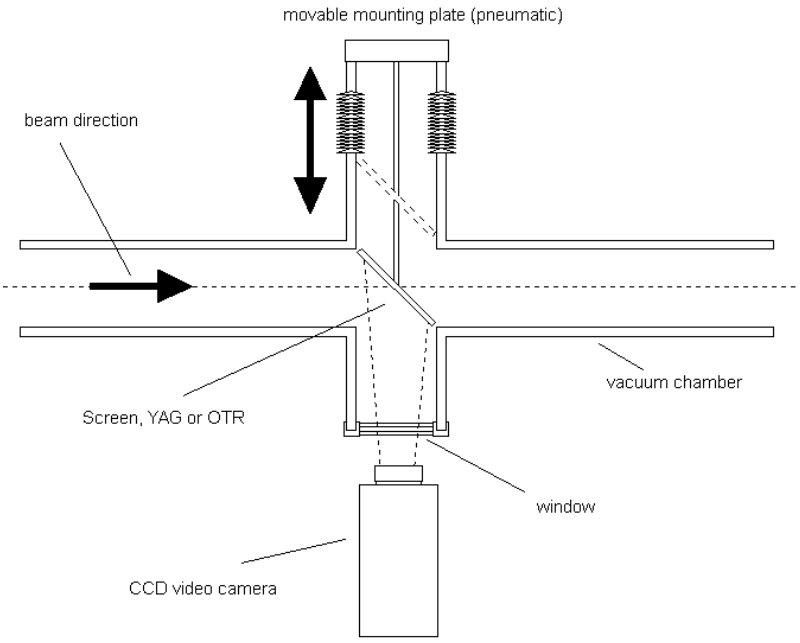

Fig.4.1. Schematic drawing of a typical screen monitor station
The screen, rotated 45° to the beam direction, emits light which can be observed by a CCD camera with a fast electronical shutter [11] *through a window in the vacuum chamber. Screens used are either a YAG (crystal scintillator) or an Al-foil producing optical transition radiation (OTR)* [4].

The spot produced by the beam passing through the screen, is observed by a CCD camera and then digitalized by a frame grabber, allowing online analysis through the SLS control system. Horizontal and vertical beam profiles are calculated by summing up the recorded intensity per pixel in every column, respectively in every row of pixels.

The analysis of the images is done online, using an ***IDL.5.1*** language application. ***IDL*** contains functions, which allow to fit curves to measured values. As the beam size corresponds to the standard deviation, it can be determined by fitting a gaussian curve to the data (see figure 4.2.).

Errors in determination of beam sizes can be estimated by making the following considerations:
An error $\Delta x = 2$ *pixel* of the measured beam size corresponds to less than 1 % of number of effective horizontal and vertical pixel [11]. The calibration factor of the screen varies within $\Delta c = 2$ *pixel per mm*. The error can be calculated with

$$\Delta\sigma = \sqrt{\sum_i \left(\frac{\partial\sigma(x_1,\ldots x_i)}{\partial x_i} \right)^2 \cdot \Delta x_i^2} = \sqrt{\left(\frac{\Delta x}{c} \right)^2 + \left(\frac{x}{c^2} \cdot \Delta c \right)^2}$$

. Hence, for a typical calibration factor of $c = 40$ *pixel per mm* and beam size $x = 50$ *pixel*, the error $\Delta\sigma$ is 0.08 mm. In the following, a uniform error of $\Delta\sigma = 0.08$ *mm* is assumed.

The dispersion can be calculated from the measured deflection x of the center of mass of the spot due to a well-known relative change of energy $\delta := \frac{\Delta E}{E}$ of the beam. The dispersion then equals $D = x/\delta$.

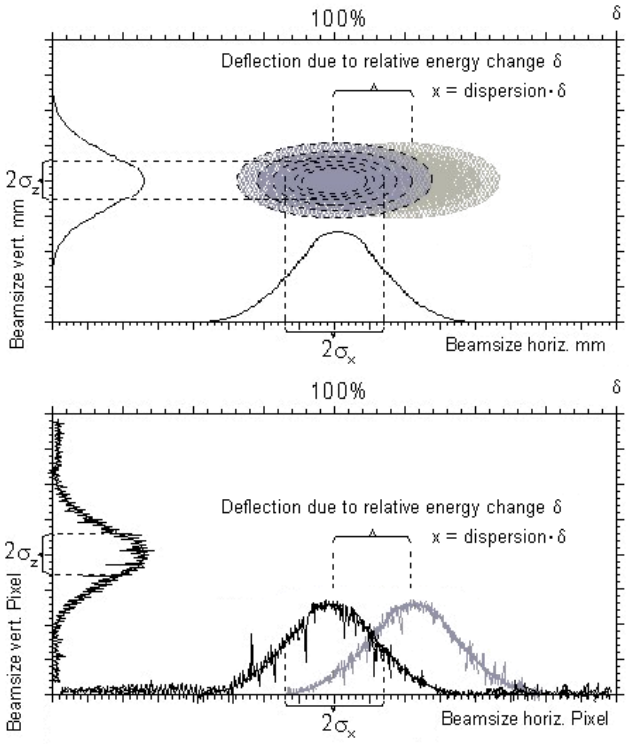

Fig. 4.2. Principles in measuring beam sizes and the dispersion for known changes of relative beam energy

The beam size is determined by fitting a gaussian curve to the measured beam profile. Dispersion can be calculated from measured deflection of the beam due to a well-known relative change in energy of the beam.

4.1. Measurement of Beam Parameters at the Linac Exit

The important parameters to be determined at the end of the pre-injector are the alpha- and beta functions, respectively the emittance of the beam. The principle of the measurement is described in chapter 3.1. [4].

As indicated in chapter 3.1, the results of the measurements show a wide range of beam parameters. It was found that the beta function varies within a range from 2 to 15 m, while the alpha values imply a divergent beam with values in the range of $-1/2$ to -4.
The normalized emittance was varying between 10 mm mrad and 60 mm mrad.
Energy spread measured at ***ALIDI-SM-E*** is changing from values smaller than 0.1 % to values higher than 0.2 %.
A representative compilation of results from different dates can be found in the appendix.

As the second part of the pre-injector can be treated as drift, it is clear that altering the quadrupole lenses ***ALIMA-QL-1/2/3*** in between of the two linac structures influences the beam parameters at the end of the linac. Therefore, it is possible to achieve conditions near to the desired ones derived

in section 3.1. without the need to alter RF phases in the linac bunching section. Leaving RF phases untouched will keep the energy spread δ constant.

Adjusting the ***QL triplet*** as follows, resulted in beam parameters listed below:

ALIMA-QL-1	1.06 A
ALIMA-QL-2	2.12 A
ALIMA-QL-3	1.18 A

Table 4.1.1. Optical functions at linac exit for adjusted QL triplet
Original values were around β = 3 m and α = -0.6 in both planes

parameter	**average value**	**standard deviation**
β_x	4.18 m	0.60 m
α_x	-1.30	0.08
ε_x normalized	16.80 mm mrad	2.71 mm mrad
β_z	7.93 m	0.80 m
α_z	-1.68	0.06
ε_z normalized	10.02 mc mm mrad	1.99 mc mm mrad

The energy spread δ was measured to be smaller than 0.1 %.

These conditions were the initial parameters during the measurement of the transversal beam sizes in the LTB presented in the following section, for the reference magnet setting in 3.2.1.

As the 90 keV electron gun is capable of emitting charges of up to 2 nC [3] it was further investigated what effect the increase of charge had on the beam parameters at the linac exit. The space charge effect dominates at lower beam energies and leads to increased beam size.
However, the measurements presented below, show that the space charge effect does not play an important role:

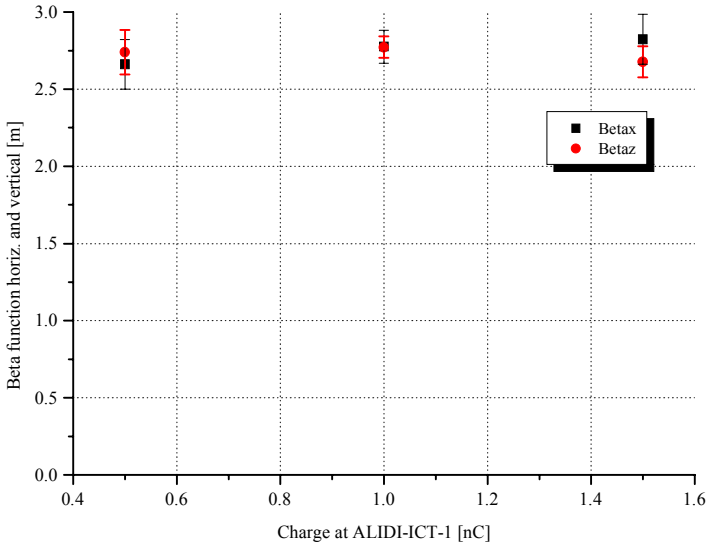

Fig. 4.1.1. Beta functions at ALIVA-VC7 dependant on charge
Error bars: standard deviation for average values; the number of measurements was 5 for each charge

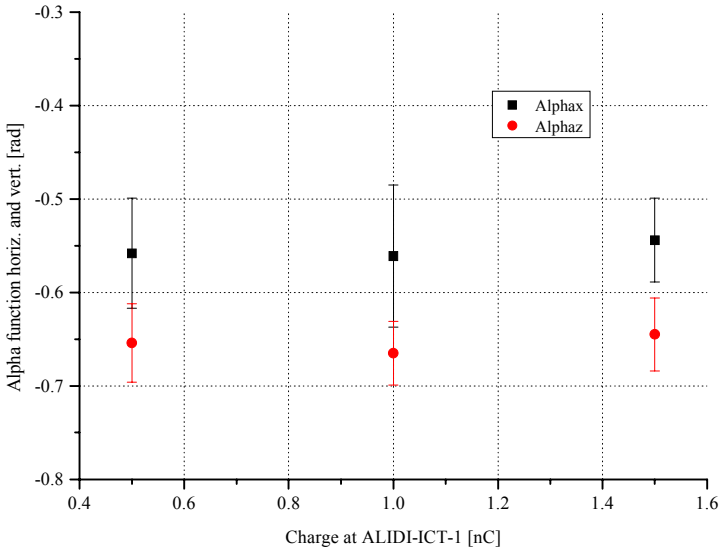

Fig. 4.1.2. Alpha functions at ALIVA- VC7 dependant on charge
Error bars: standard deviation for average values; the number of measurements was 5 for each charge

As can be seen above, measured beta- and alpha functions were not affected by the increase of the charge. Further it was found that, depicted in the following figure, the increase of the emittance also is rather small and can be neglected in further considerations.

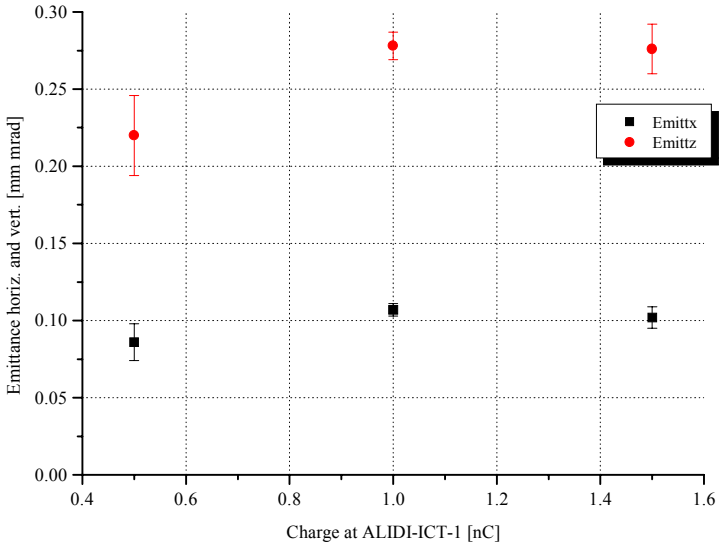

Fig. 4.1.3. Emittance at ALIVA-VC7 dependant on charge
Error bars: standard deviation for average values; the number of measurements was 5 for each charge

4. 2. Measurement of Transverse Beam Parameters in the LTB

The measurements of beam sizes and dispersion presented below are for the reference magnet setting (see table 3.2.1.2.). Initial parameters near to the reference conditions can be achieved by altering the ***ALIMA-QL*** triplet (see section 4.1.).

4.2.1. Measurements of Beam Sizes along the LTB

As can be seen in chapter 3.2. there are five screen monitors along the LTB, which allow the determination of transverse dimensions of the beam as well as dispersion. The first one ***ALIMA-SM-5*** is situated in front of the first bending magnet. The screens ***ALBDI-SM-1 and 2*** are located in the area of high dispersion before and after the second quadrupole triplet. The fourth screen ***ALBDI- SM-3*** is placed just ahead of the second bending magnet and the last one ***ALBDI-SM-4*** in front of the injection septum.

The beam size Σ can be calculated by using equation (22) $\Sigma^2 = \varepsilon \cdot \beta + (D \cdot \delta)^2$ assuming a gaussian distribution in transverse and longitudinal phase space. It can be concluded from agreement of calculated Σ with measured beam sizes that the lattice, which is the basis of the LTB simulation, corresponds with the reality.

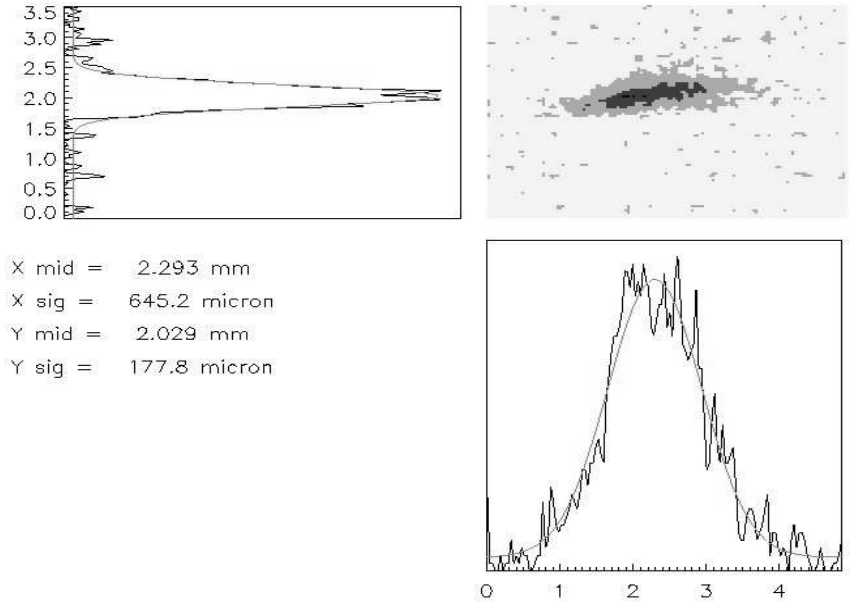

Fig. 4.2.1.1. Beam size measured at ALIDI-SM-5

$\sigma_{horiz.}^{simulated} = 700\mu m$, $\sigma_{vert.}^{simulated} = 200\mu m$

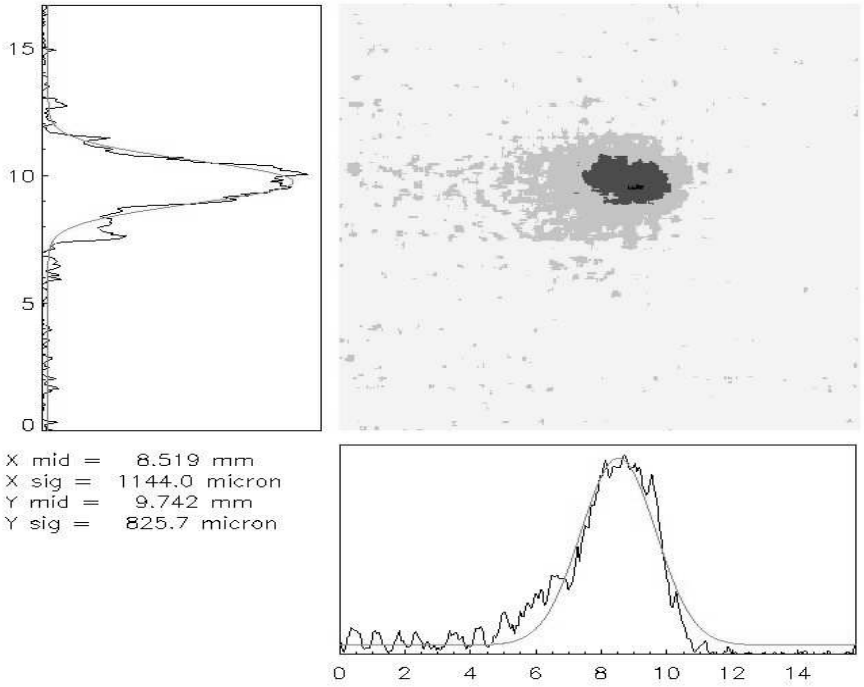

Fig. 4.2.1.2. Beam size measured at ALBDI-SM-1

$\sigma_{horiz.}^{simulated} = 1200\mu m$, $\sigma_{vert.}^{simulated} = 600\mu m$

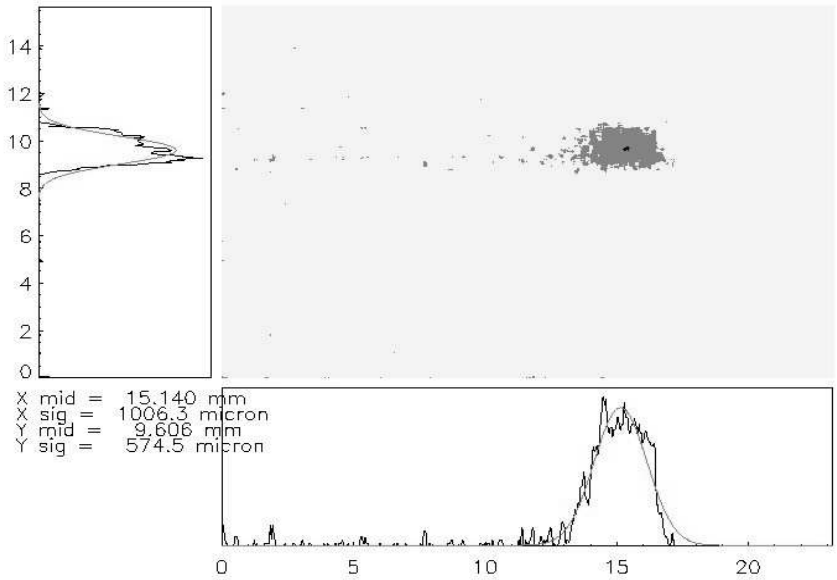

Fig. 4.2.1.3. Beam size measured at ALBDI-SM-2

$\sigma_{horiz.}^{simulated} = 900\mu m$, $\sigma_{vert.}^{simulated} = 500\mu m$

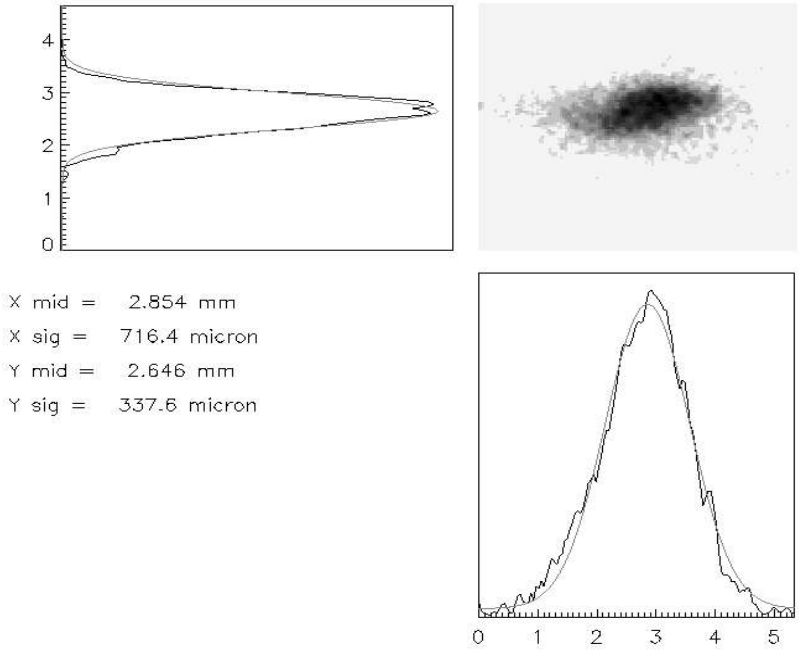

Fig. 4.2.1.4. Beam size measured at ALBDI-SM-3

$\sigma_{horiz.}^{simulated} = 800\mu m$, $\sigma_{vert.}^{simulated} = 400\mu m$

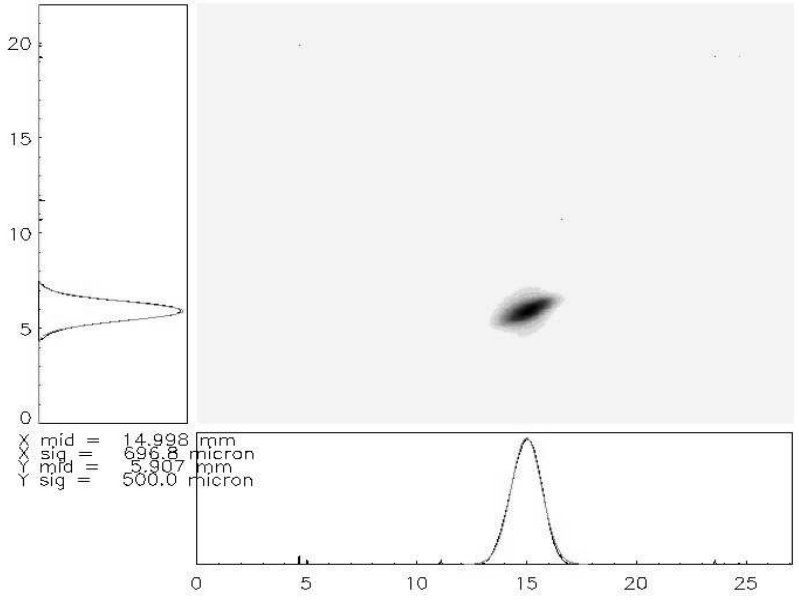

Fig. 4.2.1.5. Beam size measured at ALBDI-SM-4

$\sigma_{horiz.}^{simulated} = 600\mu m$, $\sigma_{vert.}^{simulated} = 450\mu m$

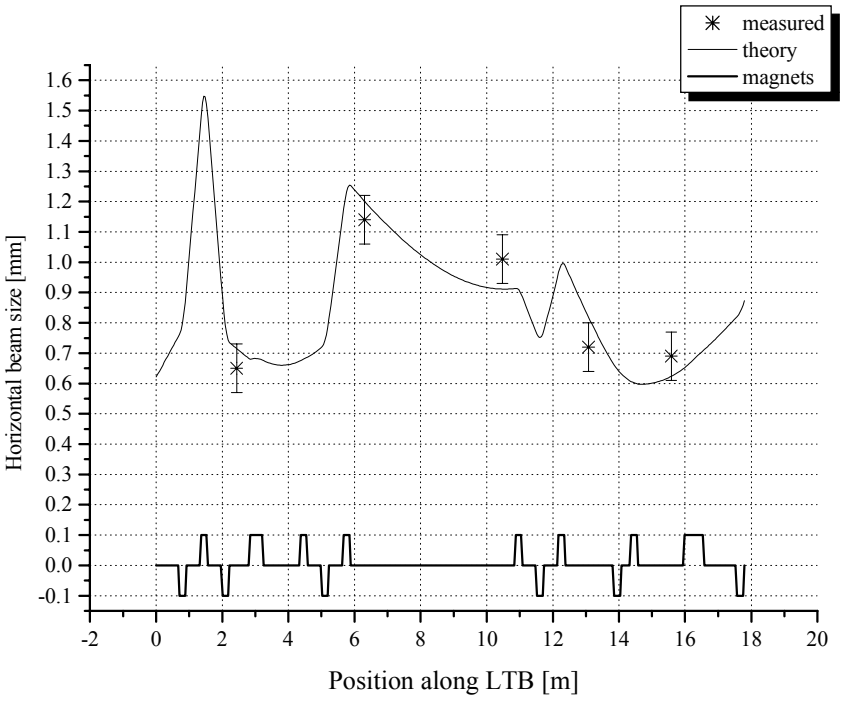

Fig. 4.2.1.6. Horizontal beam size measured versus simulated
Input parameters for the calculation are β_x = 4.2 m, α_x = -1.3, δ = 0.08 % and ε_x = 0.09 mm mrad. Error bars indicate an accuracy of 0.08 mm of measurements with the screen monitors.

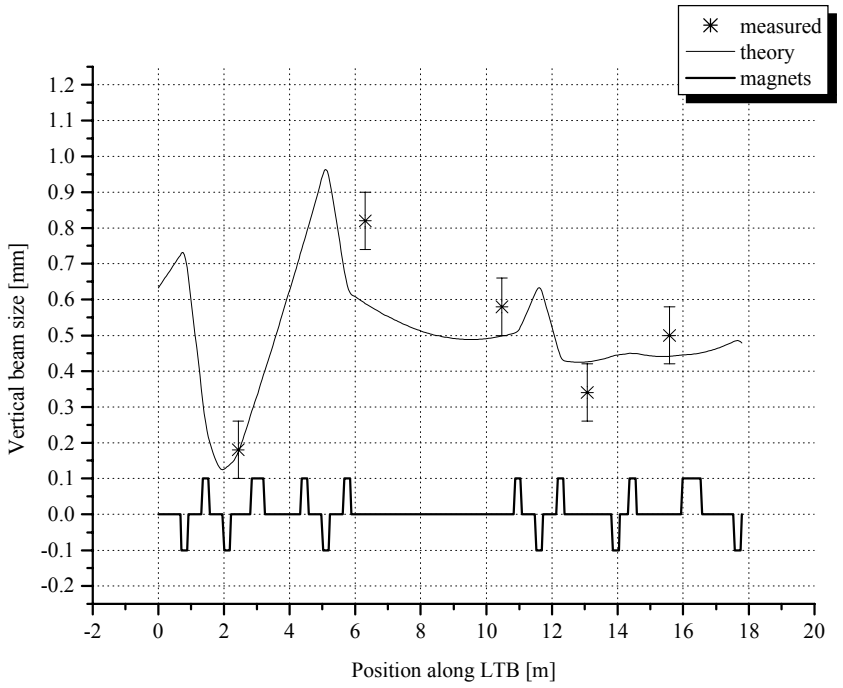

Fig. 4.2.1.7. Vertical beam size measured versus simulated
Input parameters for the calculation are β_z = 8.0 m, α_z = -1.7 and ε_z = 0.05 mm mrad. Error bars indicate an accuracy of 0.08 mm of measurements with the screen monitors.

Most of the measured values agree within the assumed measuring accuracy of 0.08 mm with the simulated beam size

4.2.2. Measurement of Dispersion

The other optical parameter, measured in the transfer line, was the dispersion. This is achieved by altering the beam energy and measuring the deflection *x* due to this change. The dispersion can then be calculated by using the equation $D = \frac{x}{\delta}$, with δ being the relative energy change $\frac{\Delta E}{E}$ (see figure 4.2.2.1).

Altering the high voltage of the klystron for the second linac structure changed the energy of the beam. Energy calibration is made by using the bending magnet ***ALIMA-BY***. An applied current of 69.335 A at ***BY*** corresponds to 100 % energy; altering the current by ±0.350 A should match with a relative energy change of ±0.5 %. This was reproducible by changing the high voltage of the klystron 2 by ±0.1 kV.

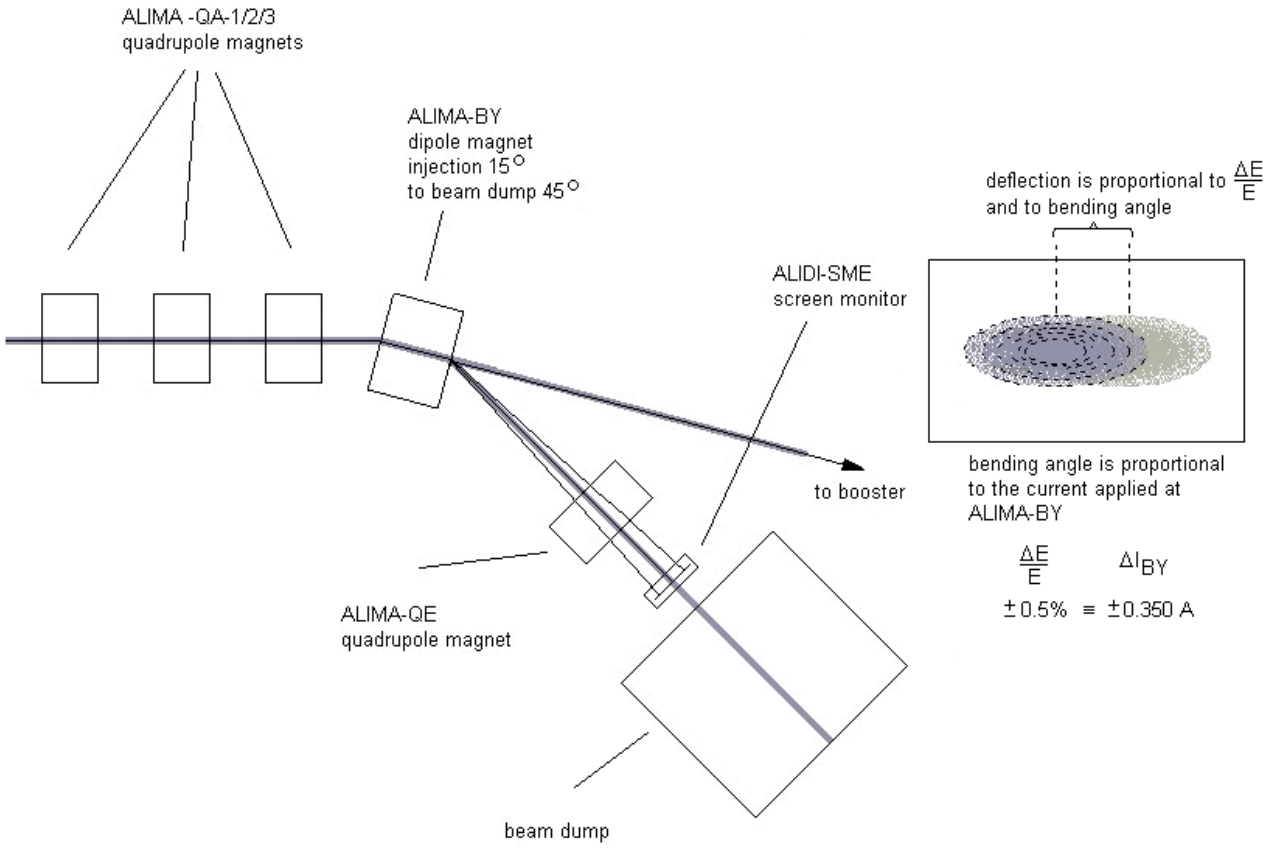

Fig. 4.2.2.1. Energy calibration at ALIDI-SME

The error in dispersion can be calculated with

$$\Delta D = \sqrt{\sum_i \left(\frac{\partial D(x_1,...x_i)}{\partial x_i} \right)^2 \cdot \Delta x_i^2} = \sqrt{\left(\frac{\Delta x}{\delta} \right)^2 + \left(\frac{x}{\delta^2} \cdot \Delta\delta \right)^2} .$$

We assume an error Δx of 0.08 mm for the deflection x and an error $\Delta\delta$ of 0.05 % in calibrating the relative energy change δ. The resulting errors are listed below:

Table 4.2.2.1. Measured dispersion and corresponding error

Screen monitor	Deflection x for δ = 1 % [mm]	Dispersion calculated [m]	Error dispersion [m]
ALIDI-SM-5	0.0	0.00	0.01
ALBDI-SM-1	11.0	1.10	0.07
ALBDI-SM-2	9.5	0.95	0.05
ALBDI-SM-3	6.5	0.65	0.03
ALBDI-SM-4	1.0	0.10	0.01

The measured values all agree within the calculated errors with the theory:

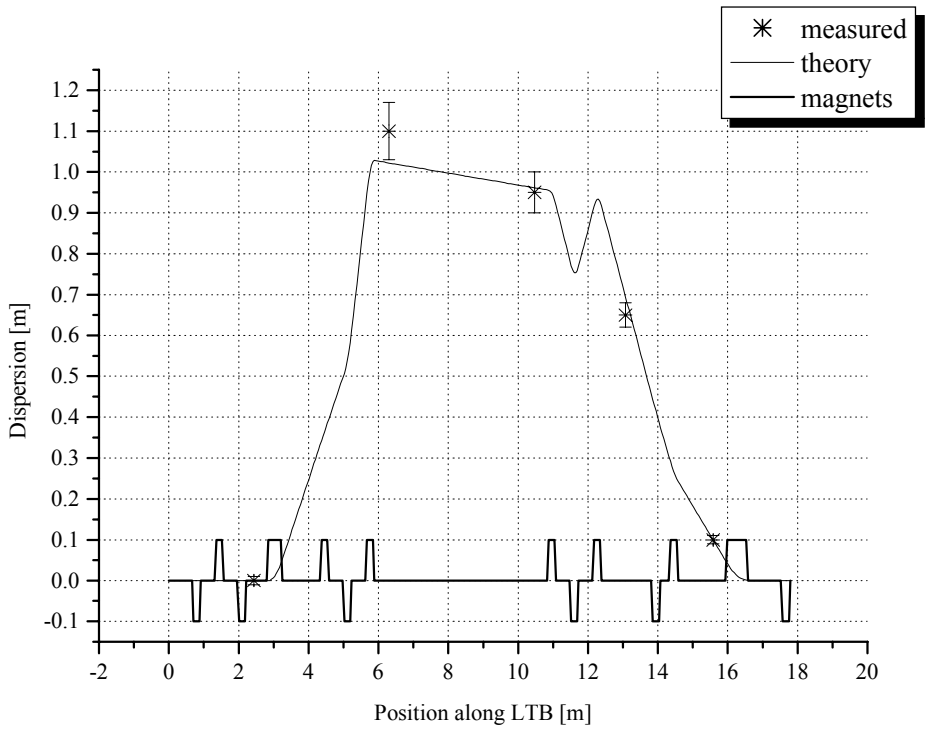

Fig. 4.2.2.2. Dispersion measured versus calculated
Error bars correspond to calculated errors; see table 4.2.2.1.

The above measurements are in good agreement with the LTB simulation. The same measurements for other magnet setting corresponding to different initial conditions (to be found in the appendix) lead to similar results. Therefore, it can be concluded that the optics in the LTB is predictable and the calculated simulations of matching are applicable.

4.3. Measuring Beta Functions in the Booster

Matching the LTB to the booster requires knowledge of optical functions in the booster synchrotron. These values are known from the calculation based on the booster design lattice. Beta functions in a circular machine can be measured in quadrupoles when altering their focusing strength and by measuring the resulting shift in tune. The following considerations describe the theoretical principles applied in the measurement [1].

According to equation (16) one can write the transformation matrix for one revolution as

$$M_{fullTurn} = \begin{pmatrix} \cos 2\pi Q + \alpha_0 \sin 2\pi Q & \beta_0 \sin 2\pi Q \\ -\gamma_0 \sin 2\pi Q & \cos 2\pi Q - \alpha_0 \sin 2\pi Q \end{pmatrix} \tag{28}$$

This follows as the initial Twiss parameters should equal to the final one for one full turn $\alpha_{initial} = \alpha_{final} = \alpha_0$, $\beta_{initial} = \beta_{final} = \beta_0$ and the phase advance ψ for one turn is of course 2πQ.

Now we consider a single quadrupole. Therefore the matrix for one revolution is written as

$$M_{fullTurn} = M_{Quad} \cdot M_{\mathrm{Re}st} \tag{29}$$

For the short piece of quadrupole with length dl it applies that $M_{Quad} = \begin{pmatrix} 1 & dl \\ -kdl & 1 \end{pmatrix}$ (30)

A quadrupole with an error of Δk is described with the matrix $M^*_{Quad} = \begin{pmatrix} 1 & dl \\ -(k+\Delta k)dl & 1 \end{pmatrix}$ (31)

As $|\Delta k \cdot dl^2| << 1$ one can write the matrix for the quadrupole with an error as

$$M^*_{Quad} = \begin{pmatrix} 1 & dl \\ -\Delta k dl & 1 \end{pmatrix} M_{Quad} \tag{32}$$

According to (29) it is

$$M^*_{fullTurn} = \begin{pmatrix} 1 & dl \\ -\Delta k dl & 1 \end{pmatrix} M_{fullTurn} \tag{33}$$

The error in focusing will produce a shift in tune ΔQ. For λ:= 2π(Q + ΔQ) we write

$$M_{fullTurn}(Q+\Delta Q) = \begin{pmatrix} \cos\lambda + \alpha_0 \sin\lambda & \beta_0 \sin\lambda \\ -\gamma_0 \sin\lambda & \cos\lambda - \alpha_0 \sin\lambda \end{pmatrix}. \tag{34}$$

$M^*_{fullTurn}$ and $M_{fullTurn}(Q + \Delta Q)$ are the same linear transformations in different coordinates. Therefore, it is necessary that $Tr(M^*_{fullTurn}) = Tr(M_{fullTurn}(Q + \Delta Q))$.

For a small shift in tune ΔQ we achieve the following valuable result:

$$\beta_i = 4\pi \frac{\Delta Q}{\Delta k \cdot dl} \tag{35}$$

Note: β_i is actually only an average <β> in the quadrupole, as the tune-shift due to the small error in focusing strength of a quadrupole of finite length l can be written as:

$$\Delta Q = \frac{1}{4\pi} \int_{s_0}^{s_0+l} \Delta k \cdot \beta(s) \cdot ds \tag{36}$$

Assuming that the error Δk is constant over the quadrupoles length one can find

$$\Delta Q = \frac{1}{4\pi}\Delta k \cdot \langle \beta \rangle \cdot l \qquad (37)$$

Because the integer part of the tune should remain constant and only the slope is of importance, solely the fractions of the tune are used. A factor of one sixth must be added, as there are six magnets in the booster lattice. Altering their strength will simultaneously change all six. Therefore, for small errors Δk the superposition-principle applies.

The measurement is performed by altering the focusing strength in ***ABOMA-QD/-QE/-QF*** and by recording the resulting tune. Then Q_{fract} is plotted as a function of the focusing strength. According to equation (37) the resulting slope, which was calculated by using the method of the least squares (with ***Origin 6.10***) [12], multiplied with $\frac{1}{6} \cdot \frac{4\pi}{l}$ gives the average beta function in the quadrupole where the focusing strength was changed.

Tunes are extracted by applying FFT to a large number (1024 samples) of turn-by-turn data delivered by a dedicated BPM station in the booster. Principles of tune measurements are described in [13].

Table 4.3.1. Fractional tune Q_x and Q_z in dependence of k at ABOMA-QD,
length 0.22 m, linear coefficient 0.3576 $A^{-1}m^{-2}$

I [A]	k [m^{-2}]	fract. tune horiz.	fract. tune vert.
-3.4002	-1.216	0.429	0.456
-3.4502	-1.234	0.423	0.464
-3.5002	-1.252	0.414	0.469
-3.5502	-1.270	0.408	0.478
-3.6002	-1.287	0.400	0.487

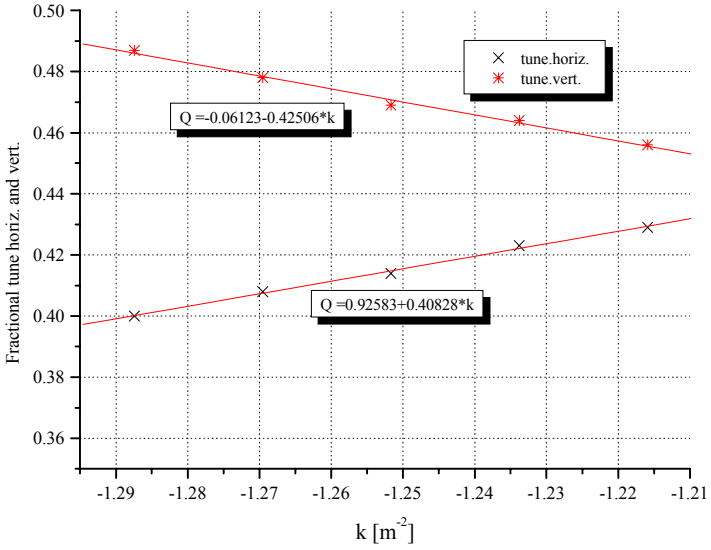

Fig. 4.3.1. Fractional tune Q_x and Q_z in dependence of k at ABOMA-QD
$\langle\beta_x\rangle^{measured} = 3.9$ m, $\langle\beta_x\rangle^{simulated} = 4.5$ m
$\langle\beta_z\rangle^{measured} = 4.0$ m, $\langle\beta_z\rangle^{simulated} = 4.2$ m

Table. 4.3.2 Fractional tune Q_x and Q_z in dependence of k at ABOMA-QE,
length 0.22 m, linear coefficient 0.3576 $A^{-1}m^{-2}$

I [A]	k [m^{-2}]	fract. tune horiz.	fract. tune vert.
-0.1700	-0.608	0.418	0.492
-0.1200	-0.429	0.422	0.470
-0.0700	-0.250	0.429	0.456
-0.0200	-0.072	0.434	0.438
+0.0300	+0.011	0.433	0.432

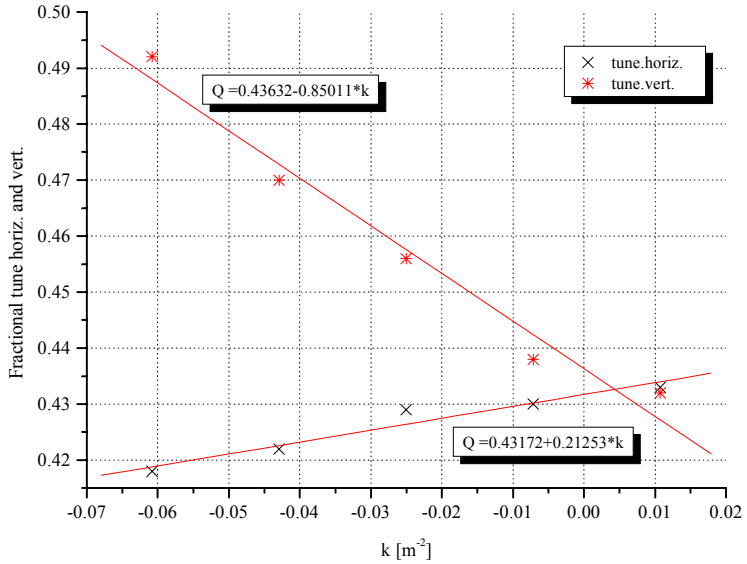

Fig. 4.3.2. Fractional tune Q_x and Q_z in dependence of k at ABOMA-QE
$<\beta_x>^{measured} = 2.0$ m, $<\beta_x>^{simulated} = 1.7$ m
$<\beta_z>^{measured} = 8.1$ m, $<\beta_z>^{simulated} = 9.4$ m

Table. 4.3.3 Fractional tune Q_x and Q_z in dependence of k at ABOMA-QF,
length 0.40 m, linear coefficient 0.3432 $A^{-1}m^{-2}$

I [A]	k [m^{-2}]	fract. tune horiz.	fract. tune vert.
4.1905	1.438	0.345	0.481
4.2405	1.455	0.381	0.470
4.2905	1.473	0.392	0.463
4.3405	1.490	0.425	0.460
4.3905	1.507	0.429	0.456

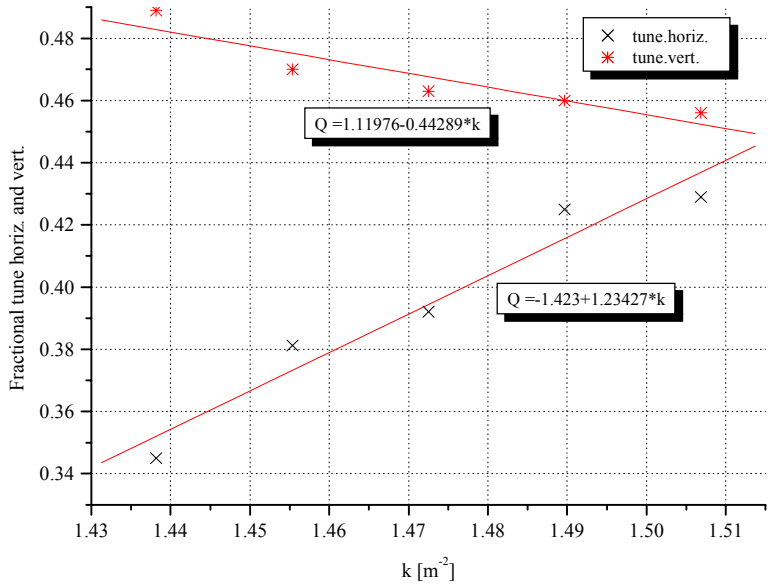

Fig. 4.3.3. Fractional tune Q_x and Q_z in dependence of k at ABOMA-QF
$<\beta_x>^{measured}$ = 6.5 m, $<\beta_x>^{simulated}$ = 10.5 m
$<\beta_z>^{measured}$ = 2.3 m, $<\beta_z>^{simulated}$ = 2.8 m

The measurement of horizontal and vertical beta function at ***ABOMA-QF*** was repeated:

Table. 4.3.4 Fractional tune Q_x and Q_z in dependence of k at ABOMA-QF,
length 0.40 m, linear coefficient 0.3432 $A^{-1}m^{-2}$

I [A]	k [m^{-2}]	fract. tune horiz.	fract. tune vert.
4.0547	1.392	0.316	0.476
4.1047	1.409	0.339	0.468
4.1547	1.426	0.377	0.462
4.2047	1.443	0.429	0.454
4.2547	1.460	0.430	0.446

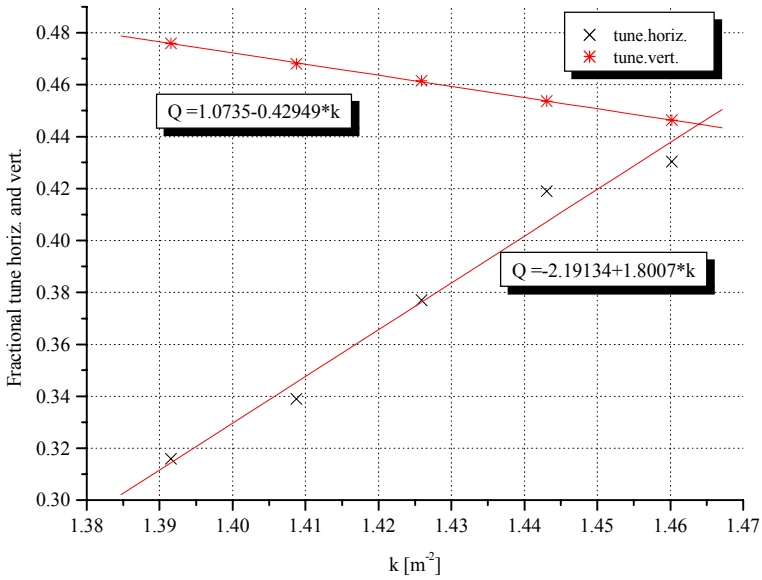

Fig. 4.3.4. Fractional tune Q_x and Q_z in dependence of k at ABOMA-QF
$<\beta_x>^{measured} = 9.4\ m$, $<\beta_x>^{simulated} = 10.5\ m$
$<\beta_z>^{measured} = 2.2\ m$, $<\beta_z>^{simulated} = 2.8\ m$

The results can be compared to earlier measurements [10]:

ABOMA-QE
$<\beta_x>^{measured} = 1.6$ m
$<\beta_z>^{measured} = 7.2$ m

ABOMA-QF
$<\beta_x>^{measured} = 10.0$ m
$<\beta_z>^{measured} = 2.4$ m

Estimate of Error in the Calculated Beta Functions

The quadrupoles have been calibrated with DC current. According to these measurements, an error of $\Delta k = 0.005\ m^{-2}$ can be assumed. These magnets are typically operated at currents up to 4 A. Thus, the error is smaller than 0.5 % with respect to the current applied. Since the accuracy is inversely proportional to the number of samples used in the FFT [14] the error in determination of the tune is estimated to be 0.001.

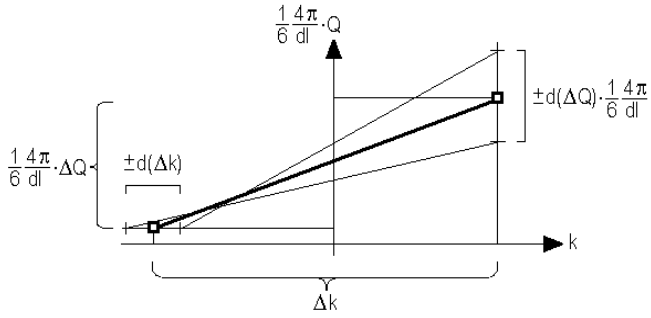

Fig. 4.3.5. Estimate of error in the beta function

Using a worst case approximation of the beta error by considering a maximum, respectively a minimum slope leads to an error in the range of 10 % to 20 %. With one exception the agreement with the design lattice is within 20 %. It is therefore admissible to assume that the optical functions in the booster correspond to the values expected by the calculation using the booster design lattice, which allows the use of the booster design lattice to match the beam envelope from the LTB.

4.4. Measurement of Transmission through the LTB and Booster/LTB Injection Efficiency

4.4.1. Measurement of Transmission through the LTB

The transmission through the LTB transfer line is constantly monitored by two integrating current transformers (***ICT***, see section 3.1.1.), one directly behind the linac and the other one in front of the booster injection septum. A typical situation, which shows the charge, emitted at the 90 keV gun (***ICT-1)*** and at ***ICT-2*** and ***ICT-3*** as well as the loss through the linac as a function of time (black curve) respectively through the LTB transfer line (green curve) is depicted below:

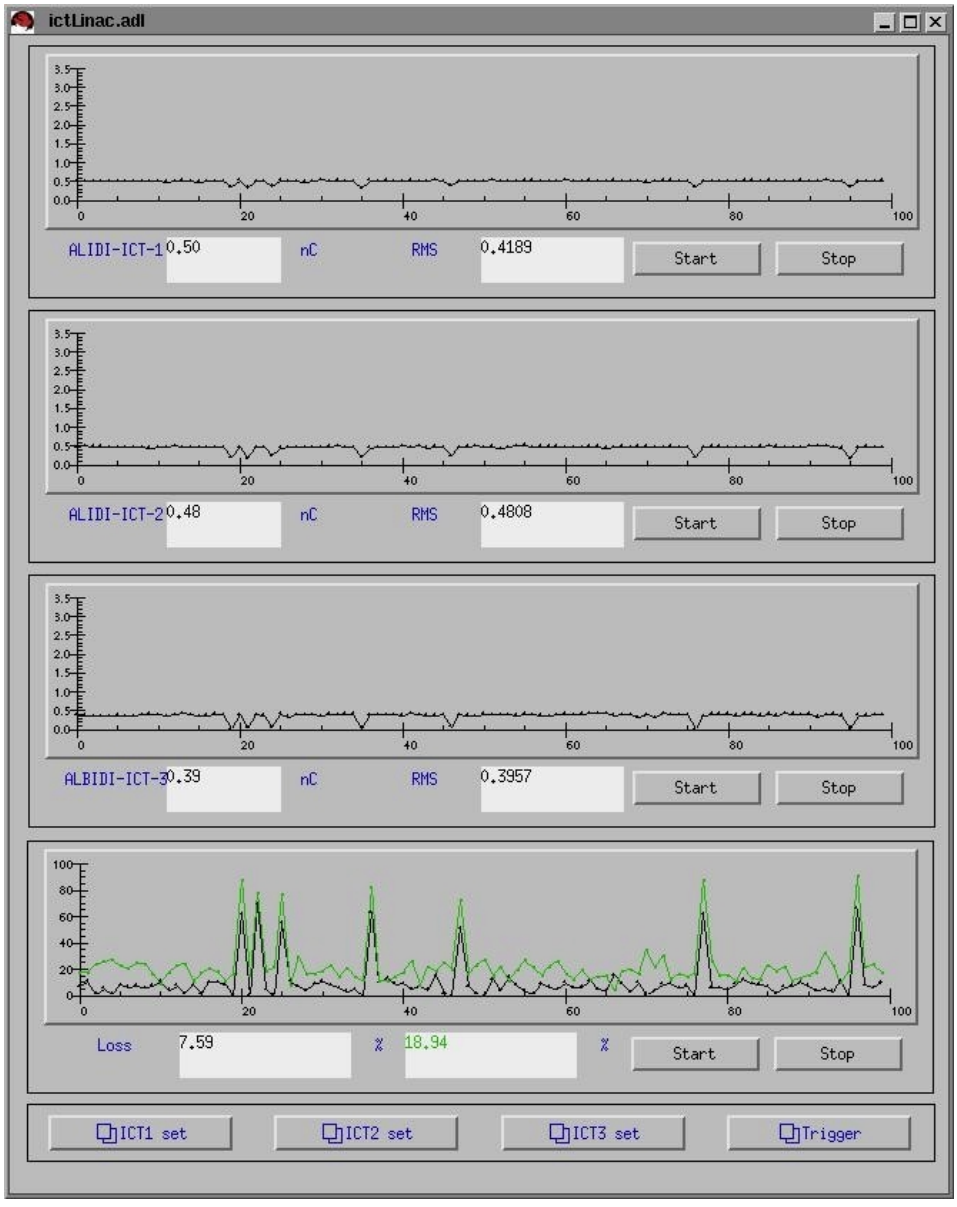

Fig. 4.4.1.1. Transmission rate through the LTB

Measured charge values in nC at ALIDI-ICT-1/2/3 are permanently compared. This measurement corresponds to a typical transmission rate through the LTB of 80 %. Improvements of more than 5 % were measured. Note drop-outs due to multi-pactoring in the subharmonic pre-buncher.

4.4.2. Measurement of the Injection Efficiency

Injected beam current in the booster synchrotron as well as transmitted current over the booster ramping cycle is monitored by means of a so-called modular parametric current transformer (MPCT) [15].

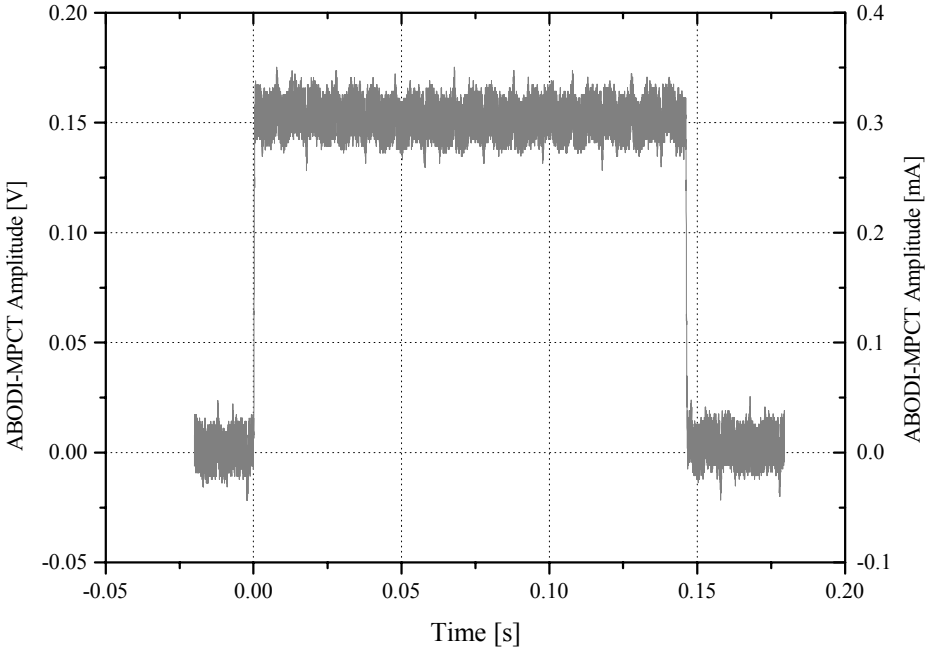

Fig. 4.4.2.1. Measurement of injection beam current in the booster during acceleration with ABODI-MPCT [15]
Calibration factor of ABODI-MPCT is k = 2 µA/mV

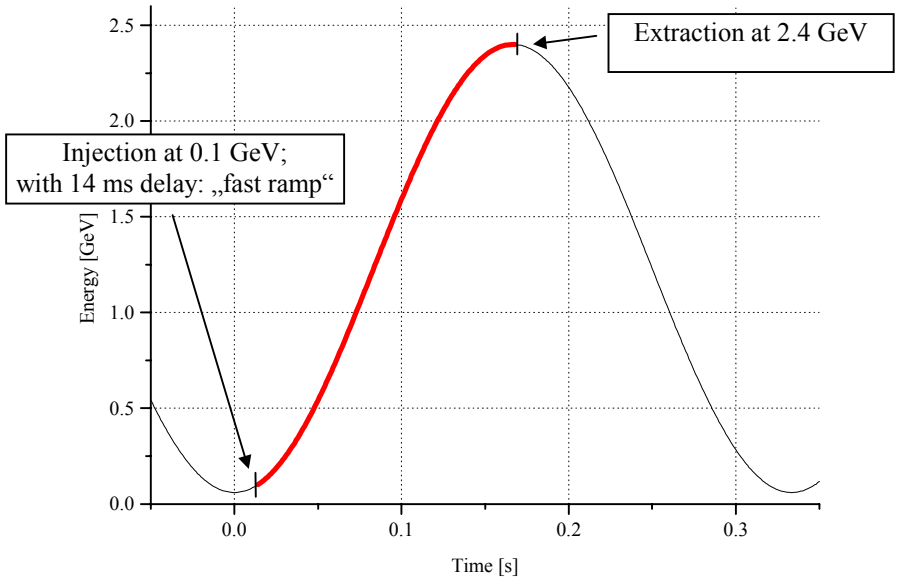

Fig. 4.4.2.2. The 3.125 Hz acceleration cycle in the booster synchrotron [10]

Electrons are traveling with the speed of light during the acceleration (0.1 GeV to 2.4 GeV). The booster circumference is 270 m, correspondingly the time for one turn in the booster synchrotron τ is calculated to be 0.9 μs.
With the Calibration factor of ABODI-MPCT, $k = 2\ \mu A/mV$, the charge injected in the booster can be determined: $Q = U \cdot k \cdot \tau$.
The measured amplitude corresponds to a charge of *0.27 nC*. Hence, with an observed charge at ALBDI-ICT-3 of 0.33 nC the injection efficiency is 82 %.

Table. 4.4.1. Transmission from linac to booster

location of charge measurement	**transmission with old matching**	**transmission with new matching**
ALIDI-ICT-1 at 4 MeV	-	-
ALIDI-ICT-2 at 100 MeV	more than 90 %	more than 90 %
ALIDI-ICT-3 in front of injection septum ABOMA-YIN	≈ 85 %	less than 95 %
ABODI-MPCT one turn in booster	≈ 75 %	≈ 85 %
ABODI-MPCT after 160 ms at 2.4 GeV	more than 90 %	more than 90 %
overall transmission from 90 keV gun to booster extraction	more than 50 %	more than 65 %

5. Conclusions and Outlook

Conclusions

The simulated settings for the quadrupoles in the LTB suggest an increase of the booster/LTB injection efficiency from 75 % to 85 %. This improvement is reproducibly achievable under present standard SLS operation conditions, when adjusting the LTB optics to the corresponding initial conditions.

It was shown by measurements of transverse beam parameters, namely beam sizes and dispersion, that the optics in the LTB transfer line is consistent with the expectations. The optical functions in the booster used to match the beam envelopes of the LTB with the one in booster agree with measured beta functions.

Hence, the observed good agreement of the real machine with the simulations supports the optimistic perspective, that the application of the new magnet settings will permanently improve the injection efficiency, if the beam conditions at the linac exit are adjusted accordingly.

Before matching of the linac with the transfer line LTB is done, the energy spread of the linac has to be optimized by altering the RF phases of the linac bunching section. The phases should not be changed afterwards to ensure a good transmission through the transfer line LTB.
Matching between linac and the transfer line LTB is then done by using the quadrupoles ***ALIMA-QL-1/2/3*** in between the two accelerating structures. For more accurate adjustments a change of the quadrupole triplet ***ALIMA-QA-1/2/3*** after the linac exit has to be considered, which will only have minor effect on the optics in the transfer line.

Outlook

In order to simplify adjustment to the required LTB settings, it should be considered to place a fourth quadrupole right after the ***ALIMA-QA-1/2/3*** triplet. The alpha- and beta functions in both horizontal and vertical plane would be easier to match with this extra knob.

6. Acknowledgement

I am grateful to my diploma professor Prof. Dr. Ralph Eichler for giving me the opportunity for an instructing and inspiring thesis at the Paul Scherrer Institut in Villigen. I would like to thank Dr. Michael Boege, Dr. Werner Joho, Dr. Leonid Rivkin, Dr. Volker Schlott and Dr. Andreas Streun for their generous efforts in teaching me a great deal about accelerator physics as well as applied measurement techniques. I am grateful for their caring supervision. I specially thank Mr. Beni Singh for our various discussions concerning numerous aspects of accelerator physics, which gave me renewed and extended inspiration for this fascinating science. I experienced a very exciting time in a kind and extremely motivating working climate during my time at the SLS, for which I would like to thank all members of the SLS. Finally, I am grateful to my parents and my sister for the tremendous support they gave me during my years of studies which enabled me to achieve my goals.

Appendix and Reference List

A.1. Abbreviations used

Table A.1.1. Abbreviations used

name	location	item
ALIDI	linac	diagnostic
ALIMA	linac	magnet
ALIVA	linac	vacuum
ALBDI	LTB	diagnostic
ALBDI	LTB	magnet
ABODI	booster	diagnostic
ABOMA	booster	magnet

A.2. Compilation of Measurements of Beam Parameters at Linac Exit

Table A.2.1. Optical functions at linac exit, 30. May 2001
Charge at ICT-1 was 1.5 nC ± 0.2 nC, 5 measurements were performed using the YAG screen

parameter	average value	standard deviation
β_x	7.15 m	0.68 m
α_x	-1.45	0.23
ε_x normalized	16.24 mm mrad	6.55 mm mrad
β_z	7.09	0.98
α_z	-1.47	0.34
ε_z normalized	24.44 mm mrad	11.52 mc mm mrad

Table A.2.2. Optical functions at linac exit, 21. June 2001
Charge at ICT-1 was 0.5 nC ± 0.1 nC, 5 measurements were performed using the YAG screen

parameter	average value	standard deviation
β_x	12.52 m	0.95 m
α_x	-2.97	0.18
ε_x normalized	11.54 mm mrad	0.97 mm mrad
β_z	14.76	0.56
α_z	-2.89	0.10
ε_z normalized	11.94 mm mrad	1.29 mm mrad

Table A.2.3. Optical functions at linac exit, 05. July 2001

Charge at ICT-1 was 0.5 nC ± 0.1 nC, 10 measurements were performed using the YAG screen

parameter	average value	standard deviation
β_x	10.10 m	1.18 m
α_x	-1.82	0.28
ε_x normalized	9.09 mm mrad	2.12 mm mrad
β_z	6.24 m	0.85
α_z	-1.34	0.20
ε_z normalized	12.33 mm mrad	1.28 mm mrad

Table A.2.4. Optical functions at linac exit, 10. July 2001

Charge at ICT-1 was 0.5 nC ± 0.1 nC, 5 measurements were performed using the YAG screen

parameter	average value	standard deviation
β_x	2.66 m	0.16 m
α_x	-0.56	0.06
ε_x normalized	16.80 mm mrad	2.43 mm mrad
β_z	2.74 m	0.15
α_z	-0.65	0.04
ε_z normalized	43.12 c mm mrad	5.09 mm mrad

Table A.2.5. Optical functions at linac exit, 16. July 2001

Charge at ICT-1 was 0.5 nC ± 0.1 nC, 5 measurements were performed using the YAG screen

parameter	average value	standard deviation
β_x	2.75 m	0.08 m
α_x	-0.56	0.03
ε_x normalized	20.02 mm mrad	0.41 mm mrad
β_z	2.72 m	0.13
α_z	-0.68	0.02
ε_z normalized	52.00 mm mrad	1.78 mm mrad

Table A.2.6. Optical functions at linac exit, 13. August 2001

Charge at ICT-1 was 0.5 nC ± 0.1 nC, 5 measurements were performed using the YAG screen

parameter	average value	standard deviation
β_x	4.18 m	0.60 m
α_x	-1.30	0.08
ε_x normalized	16.80 mm mrad	2.71 mm mrad
β_z	7.93 m	0.80 m
α_z	-1.68	0.06
ε_z normalized	10.02 mm mrad	1.99 mm mrad

A.3. Additional LTB Magnet settings

Table A.3.1. Optical functions in the LTB simulated with AGILE for condition 1:
$\beta_{x,z} = 12$ *m;* $\alpha_{x,z} = -2.5$

Opt. function	Screen monitor ALIDI-SM-5	Screen monitor ALBDI-SM-1	Screen monitor ALBDI-SM-2	Screen monitor ALBDI-SM-3	Screen monitor ALBDI-SM-4
β_x [m]	7.99	3.14	10.37	7.40	4.11
α_x [rad]	2.67	-0.18	-1.55	1.28	0.20
β_z [m]	0.49	17.85	5.24	4.13	3.97
α_z [rad]	1.75	2.19	0.84	-0.05	0.08
D_x [m]	0.00	1.08	1.29	0.69	0.10
dD_x/ds [rad]	0.00	0.05	0.05	-0.32	-0.14

Table A.3.2. Calculated focusing strengths and currents for condition 1

Magnet	k [m^{-2}]	I [A]
ALIMA-QA-1	-5.236	-25.793
ALIMA-QA-2	8.157	40.182
ALIMA-QA-3	-8.362	-41.192
ALBMA-QB-1	0.177	0.872
ALBMA-QB-2	-4.817	-23.729
ALBMA-QB-3	3.484	17.163
ALBMA-QC-1	2.408	11.862
ALBMA-QC-2	-3.224	-15.882
ALBMA-QC-3	1.835	9.039
ALBMA-QI	-0.300	-0.840

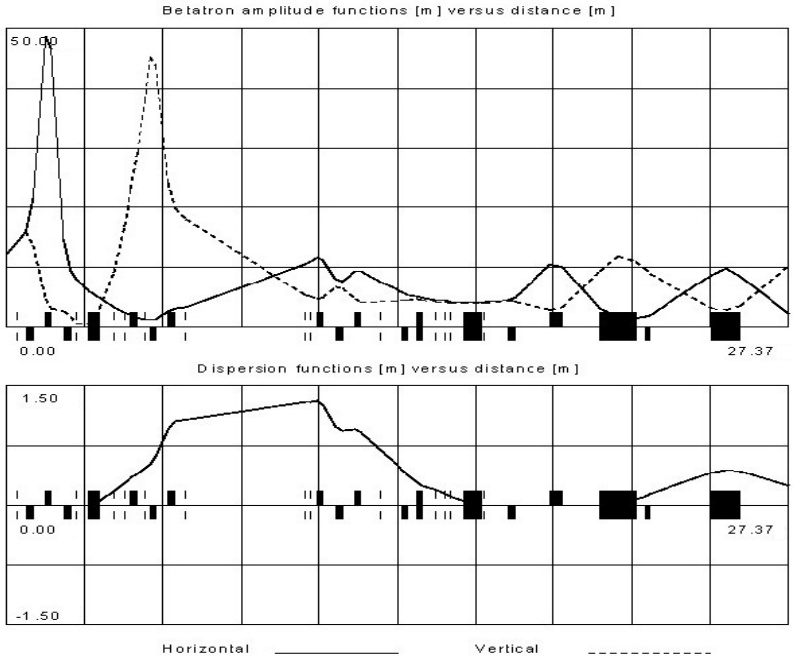

Fig. A.3.1. Display of optical functions along LTB up to booster entrance using GUI for condition 1

Table A.3.3. Optical functions in the LTB simulated with AGILE for condition 2:
$\beta_{x,z} = 3$ *m;* $\alpha_{x,z} = -0.75$

Opt. function	Screen monitor ALIDI-SM-5	Screen monitor ALBDI-SM-1	Screen monitor ALBDI-SM-2	Screen monitor ALBDI-SM-3	Screen monitor ALBDI-SM-4
β_x [m]	5.01	11.10	1.58	7.41	4.12
α_x [rad]	-0.04	2.57	-0.28	1.28	0.20
β_z [m]	0.77	2.70	6.42	4.14	3.96
α_z [rad]	0.04	0.63	1.52	-0.05	0.08
D_x [m]	0.00	0.94	0.71	0.68	0.09
dD_x/ds [rad]	0.00	-0.06	-0.06	-0.32	-0.14

Table A.3.4. Calculated focusing strengths and currents for condition 2

Magnet	k [m^{-2}]	I [A]
ALIMA-QA-1	-6.328	-31.172
ALIMA-QA-2	7.890	38.867
ALIMA-QA-3	-6.792	-33.458
ALBMA-QB-1	1.259	6.202
ALBMA-QB-2	-5.751	-28.330
ALBMA-QB-3	4.135	20.369
ALBMA-QC-1	0.110	0.542
ALBMA-QC-2	-3.942	-19.419
ALBMA-QC-3	4.132	20.355
ALBMA-QI	-0.300	-0.840

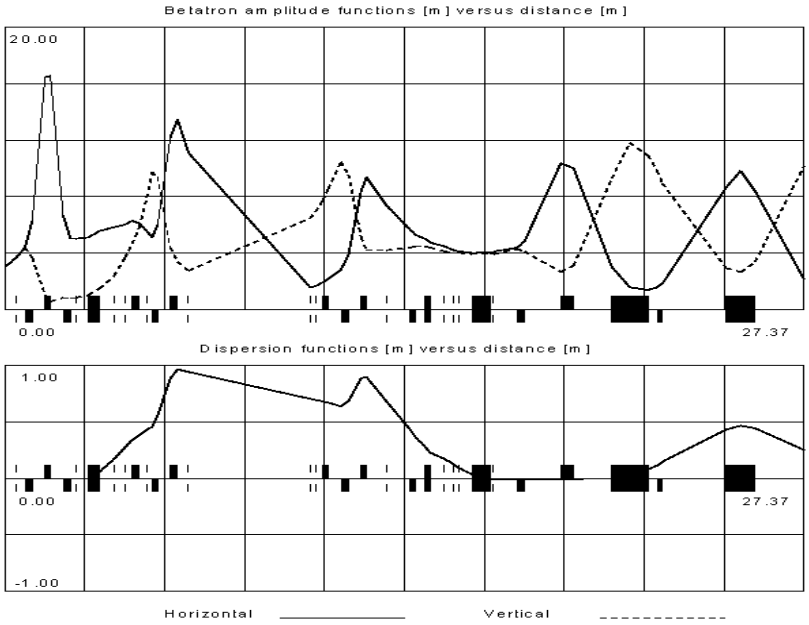

Fig. A.3.2. Display of optical functions along LTB up to booster entrance using GUI for condition 2

A.4. Integrating Current Transformer (ICT)

The ICT's used are standard commercial diagnostic devices [15], which are fundamentally acting like current transformers having a tape wound core of high permeability metal alloy. The beam represents the single primary turn. The SLS ICT's have 5 turns on the second winding, where 1/5 of the beam current should flow (5 times the voltage). Thus, integrating the current in the transformer circuit over the bunch duration measures exactly 1/5 of the beam charge.

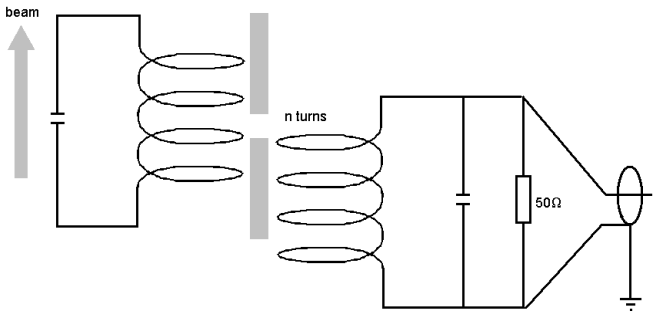

Fig. A.4.1. Operation principle of the integrating current transformer
The integrating current transformer is a passive transformer designed to measure the charge in a very fast pulse with high accuracy. It is capable of integrating a pulse with rise time in the order of picoseconds without signal loss.

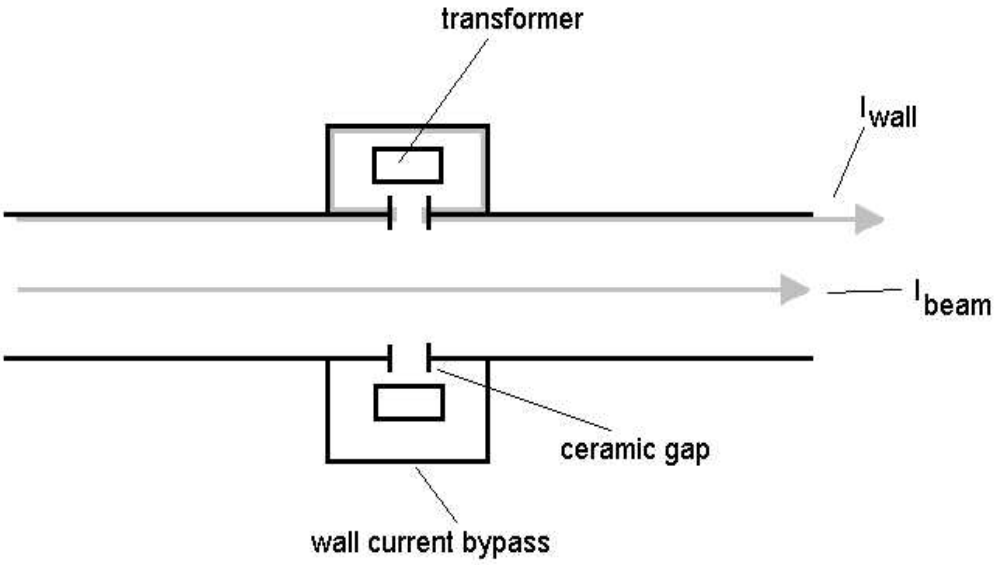

Fig. A.4.2. Keeping high harmonics of the beam out of the cavity
The transformer, the gap capacitance and the wall current bypass form together a cavity. It is important to prevent unnecessary harmonics from entering the cavity. The transformer sees the wall current. The higher frequencies of the wall current spectrum will pass through the capacitance of the ceramic gap, while the lower frequencies will enter the cavity and induce a flux in the transformer core.

Calibration of the ICT is made online, using a pulse charge generator. The generator provides pulses at ca. ± 2 % from 1pC, 10 pC, 100 pC up to 1 nC.

Reference List

[1] K. Wille, "Physik der Teilchenbeschleuniger und Synchrotronstrahlungsquellen", Teubner 1996.

[2] E. J. N. Wilson, "Circular Accelerators – Transverse" AIP Conf. Proc 153, Physics of Particle Accelerators / SLAC Summer School 1985, Fermilab, Summer School 1984.

[3] M. Pedrozzi, "SLS Pre-Injector", PSI Scientific Report 2000 / Volume VII

[4] V. Schlott et al., "SLS Linac – Commissioning Results", BIW 2000

[5] "Interactive Digital Language", version 5.1., by Research Systems Inc.

[6] P. J. Bryant, AC Division CERN, Geneva "AGILE", version 3.5.

[7] K. L. Brown et al., "TRANSPORT a Computer Program for Designing Charged Particle Beam Transport Systems", CERN, Geneva.

[8] L. M. Young, "PARMELA, Phases And Radial Motion in Electron Linear Accelerators", Los Alamos National Laboratories.

[9] A. Streun, "OPA, version 2.1. ", PSI 1997.

[10] W. Joho, "SLS Booster at its Design Performance", PSI Scientific Report 2000 / Volume VII

[11] "Sony XC-55/55BB Application Guide"

[12] "ORIGIN", version 6.1., by Origin Lab. Cooperation.

[13] M. Serio, "Transverse Betatron Tune Measurement", INFN, Frascati Roma 1989.

[14] W. H. Press et al., "Numerical Recipes", Cambridge 1989.

[15] "Modular Parametric Current Transformer" and "Integrating Current Transformer" from Bergoz Precision Instrumentation, France.